# Phase-field model of cellular migration: Three-dimensional simulations in fibrous networks

Adrian Moure[a,*], Hector Gomez[b]

[a]*Departamento de Métodos Matemáticos, Universidade da Coruña, Campus de Elviña, 15071, A Coruña, Spain*
[b]*School of Mechanical Engineering, Purdue University, 585 Purdue Mall, West Lafayette, IN 47907, U.S.A.*

**Abstract**

Cell motion plays a key role in many biological processes. Computational models are gaining momentum as a tool that allows a quantitative understanding of the main biological mechanisms of cell motility and produce testable hypotheses. Here, we present a phase-field model of the spontaneous motion of a single cell. The model, which uses a single fixed mesh only, accounts for a generic membrane-bound activator as well as actin and myosin inside the cell. The biochemical interactions between the cellular agents are described through dynamic, nonlinear partial-differential equations. These equations are coupled with a momentum balance law that accounts for the forces involved in cell motion. We propose a computational method based on isogeometric analysis. We show numerical examples corresponding to stationary states of *keratocytes* and dynamic motion of *Dictyostelium* with and without obstacles. We present a three-dimensional example of cell motion within a fibrous network of obstacles. This simulation is seen as a preliminary step for the computational study of cellular migration in the extracellular matrix.

*Keywords:* Isogeometric analysis, Phase-field method, Cell motility, Amoeboid motion

## 1. Introduction

### 1.1. Cell motility

Cell motion is a prerequisite for life. Motion manifests itself at different scales, e.g., subcellular, cellular, and tissue scales. There are cells that swim using cilia or flagella, but most eukaryotic cells produce motion using filaments that constitute the so-called cytoskeleton. Cellular motion is a tightly regulated action that plays a crucial role in several biological processes such as tissue formation, wound healing, and immune response. Thus, it is not surprising that an abnormal behavior of motile cells may lead to serious conditions, including vascular disease and cancer metastasis. For example, metastatic disease is usually preceded by the so-called epithelial-to-mesenchymal transition, whereby an epithelial cell acquires a migratory phenotype. In this process, the migratory cell has to move through the extracellular matrix, interacting with numerous collagen fibers. This process is exceedingly complex and is by no means well understood. However, a new super-resolved fluorescence microscopy has recently permitted to image a neutrophilic HL-60 cell migrating through a three-dimensional collagen matrix [1]. This discovery led to a Nobel Prize in 2014.

A key ingredient for cellular motility is actin, a family of globular proteins. These proteins have the ability to assemble into filaments through a process called polymerization. Actin filaments exert forces on the cell's membrane, producing protrusions mostly in its front part. Another key element of the motion process is myosin. The main function of myosin is the conversion of energy into mechanical force. Myosins comprise a large family of motor proteins. We are primarily interested in non-muscle myosin II, which is the most relevant myosin isoform for cell motility. Myosin II is usually located in the back of the cell and propels itself along actin filaments producing contractile stresses.
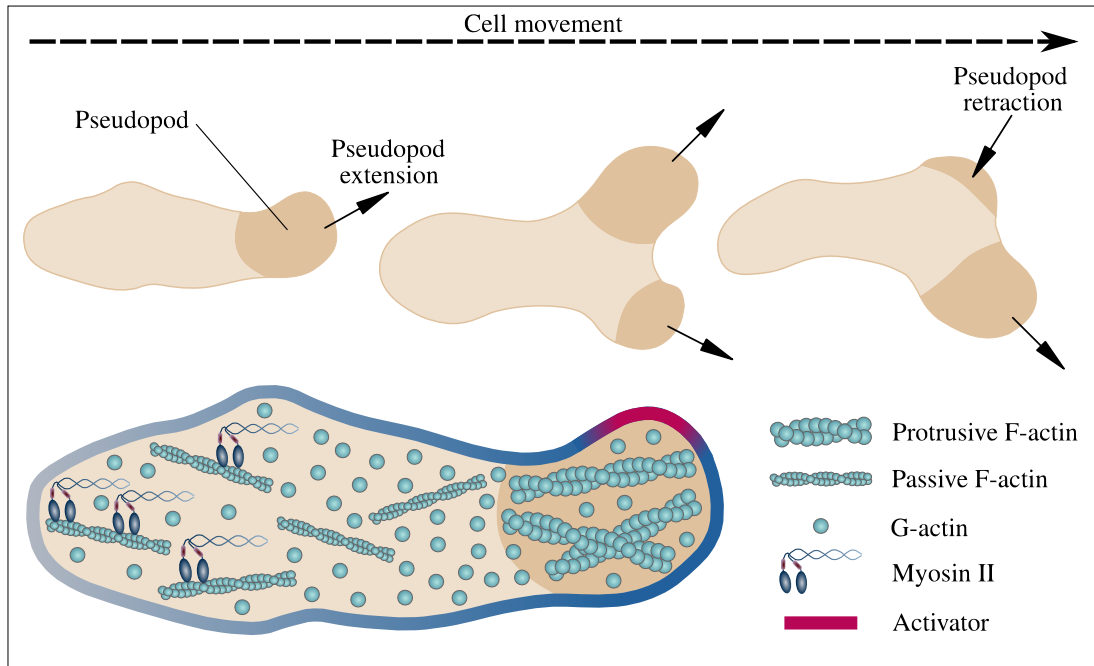
---

Figure 1: Amoeboid motion is produced by periodic extensions/retractions of pseudopods at the cell's front and contractions at the cell's rear. The bottom part of the figure shows the main elements of our model.

In general, cell migration may be understood as a continuous process including five steps [2], namely, (1) protrusion of the leading edge produced by actin polymerization, (2) formation of focal contacts and cell-matrix interaction (3) extracellular matrix degradation, (4) contraction generated by myosin, and (5) detachment of the trailing edge. While more details about cellular migration through the extracellular matrix are being unveiled, most research on cell motion is performed using simplified systems. The most classical one is the planar motion of a single cell on a flat substrate, which has attracted significant attention in the experimental and computational communities. An example of particular interest is that of amoeboid migration. In this paper, we propose a phase-field model of amoeboid migration. By using our model and suitable computational methods, we initiate the study of amoeboid cell migration in three-dimensional fibrous environments. We believe that modeling cellular migration in three-dimensional fibrous networks may constitute a first step toward the computational study of cellular motion in the extracellular matrix.

### 1.2. Amoeboid motion

Amoeboid motion is the most frequent migration mode of eukaryotic cells. It is often studied by performing experiments with *Dictyostelium discoideum*, an elongated and deformable cell that uses this type of locomotion. Amoeboid migration is a crawling-like type of motion that is enabled by protruding and retracting extensions called *pseudopods*. Pseudopods are actin-rich protrusions that push forward the leading edge of the cell. They grow and regress periodically at different points of the cell giving rise to a highly orchestrated process. The dynamic nature of pseudopods may be attributed to the ability of actin to assemble and disassemble quickly. Actin may be in a globular state (G-actin) or polymerize to give rise to a filamentous state (F-actin); see Fig. 1. In turn, F-actin can be organized into *protrusive* or *passive* structures. The protrusive structures actively push the membrane forward and are associated with pseudopods in our model.

The growth of pseudopods and the organization of F-actin into protrusive and passive structures is controlled by membrane signaling molecules, such as for example, PIP3 [3]. These substances are bound to the cell's membrane. In our model, they are conceptualized as a single substance that undergoes biochemical reactions within the membrane. We call this substance *activator*; see Fig. 1. The final ingredient to produce motion is myosin, which contracts the back part of the cell. The organized combination of protrusions at the front and contractions at the rear produces crawling-like motion.

## 1.3. Computational challenges

The three-dimensional simulation of cellular motion poses a number of computational challenges. The transport and phase transformations of actin need to be resolved on the cell's interior, which is a moving and deformable domain. The biochemical reactions inside the cell need to be coupled with the membrane mechanics. And finally, the activator is transported and undergoes biochemical reactions within the cell's membrane. The equations that govern the membrane mechanics include higher-order derivatives in space, posing significant challenges for classical finite element methods that use $C^0$-continuous basis functions. The traditional computational approach would be to solve the three-dimensional equations that govern the biochemomechanical processes on the cell's interior using a moving-mesh method. This problem would be coupled to partial-differential equations (PDEs) posed on a moving surface representing the membrane that control the dynamics of the activator. Here, we propose a computational method entirely based on the phase-field theory. The phase-field method is an emerging technology in computational mechanics for the treatment of problems with interfaces [4]. Phase-field modeling may be thought of as a methodology to reformulate problems with interfaces as partial-differential equations on fixed domains. Roughly speaking, sharp interfaces are replaced with the so-called diffuse interfaces, which are described by a smooth field defined on a fixed domain. The approach is mathematically rigorous, and in many cases the phase-field theory may be shown to converge to its corresponding moving boundary problem as a regularization parameter tends to zero. The phase-field method has been used to model, e.g., liquid-vapor phase transformations [5] or solid-solid martensitic transformations [6]. The phase-field theory can also be used to solve PDEs on complicated geometries without generating a mesh conforming to the computational domain. This approach is based on ideas similar to those employed in immersed boundary methods [7] and is known in the phase-field community as diffuse domain method. In the present work, we use the phase-field method for both purposes; modeling phase transformations and solving PDEs on the time-dependent cell geometry without generating a mesh conforming to the cell shape. To be able to follow the derivations in the paper, basic knowledge about the phase-field method and the diffuse domain approach is needed; see, for example, [4] and [8].

## 1.4. Brief bibliographic survey

Early experimental works analyzed cell-motion patterns [9, 10] describing walk models through velocity, persistence time, or contact distributions. New experimental techniques [1, 11] have lead to more detailed studies, where the modes of cell motion [2, 12, 13, 14] and the cytosol dynamics [15, 16, 17, 18] are explained, as well as the regulatory systems involved in the membrane signaling pathways [19, 20, 21]. Those experimental works have allowed to understand the main mechanisms of cell motility, though there is still a great lack of knowledge.

Computational modeling has been recently proposed as an effective way to test conceptual models of cell motility. Mathematical models may be classified according to their scale, namely, subcellular, cellular, and tissue-level. Subcellular models explain particular processes occurring at some regions of the cell, such as actin polymerization [22], actomyosin networks [23], or cell-substrate adhesion [19, 24]. Cellular-scale models simulate the entire cell. This kind of models may focus either on the membrane molecules dynamics [25, 26], on the laws governing the cytosolic components [27, 28, 29], or couple both compartments including the interaction between the cytosolic and membrane compounds [30, 31]. Tissue-level models represent collective cell motion. Some of them consider each cell as an individual behaving under certain rules [32, 33], while others treat the cell population under the assumptions of continuum mechanics [34, 35].

From the computational point of view, another classification arises attending to the methodology employed to track the cell. Some studies assume that the geometry of the cell remains constant during motion. For example, in [36] the adhesion molecules, F-actin, and myosin distributions during motion are evaluated on a fixed and non-deformable cell. Other works [25, 37, 38] have studied the time evolution of membrane-bound proteins by placing some constituents (e.g., an activator along with global and local inhibitors) on a fixed membrane. However, most models consider deformable cells. An important example is that of immersed fluid-structure interaction (FSI) algorithms [39, 40], where a Lagrangian mesh accounting for the cell moves over an Eulerian mesh that spans the whole domain. This method has allowed the incorporation of different cellular properties such as the poroelasticity of the cytoskeleton [41]. Immersed FSI methods alone are unable to account for membrane signaling components, whose importance in cell motility is well known. Therefore, the solution of PDEs on deformable surfaces [42, 43] and the membrane-cytosol interactions have drawn the attention of many authors. Similarly, FSI formulations based on Arbitrary Lagrangian

Eulerian (ALE) descriptions applied to cell migration may be found in [44, 45]. Particularly, in [44] the membrane-bound species interact with an extracellular chemoattractant ligand. In these cases, the model only determines the normal velocity and/or the forces located at the membrane, but the cytosolic machinery is neglected.

The use of moving meshes may be bypassed by several techniques, which also enable the treatment of membrane and cellular elements. In our opinion, the most significant ones are the level set and the phase-field methods. In the level set method, a distance map is placed on a fixed domain and evolves in time according to a given velocity. The distance function defines the location of the cell membrane. A significant example is [46], where a finite volume method is used to solve the problem. However, we believe that the phase-field method is more advantageous, because, as we show in this paper, the compounds may be naturally tracked and located inside, outside the cell, and at the membrane. In recent years several models have used phase-field descriptions to establish evolution equations for the main actors of cell motility [27, 47, 48]. Some works suggest that actin filament polarity controls the dynamics of the cell. For example, [49, 50] couple polarity to adhesion, nucleation factors, myosin, or traction on deformable substrates. Other recent phase-field approaches have included the actin network, modeling it as a viscous fluid [28, 51, 52] governed by a Stokes-type equation that takes into account the cell motion forces. We have recently proposed a model [30] that includes the membrane signaling reactions and couples them to the myosin and actin network. This approach allows to consider the interaction between membrane and cytosol in motile cells. More details about cellular motility models can be found at the reviews [53, 54].

## 2. Phase-field model of amoeboid cellular motion

Our model may be divided into three main compartments describing the cell's motion, the cytosol biochemomechanics and the activator dynamics. In what follows, we describe each of these compartments separately.

### 2.1. Cell motion

To define the cell location, we employ the phase-field variable $\phi(\boldsymbol{x}, t)$ where $t$ denotes time and $\boldsymbol{x} \in \mathbb{R}^{d_s}$ is a point in a space of $d_s$ dimensions. The function $\phi$ undergoes a smooth but quick transition from 0 (outside the cell) to 1 (inside the cell); see Fig. 2. To leading order $\phi$ takes a hyperbolic tangent profile in the direction normal to the cell's membrane. The membrane is associated to the diffuse interface defined by the phase field. The dynamics of $\phi$ are governed by the equation

$$\frac{\partial \phi}{\partial t} + \boldsymbol{u} \cdot \nabla \phi = \Gamma_\phi \left( \varepsilon \nabla^2 \phi - \frac{G'(\phi)}{\varepsilon} + c\varepsilon |\nabla \phi| \right), \tag{1}$$

where $\Gamma_\phi$ is a parameter setting the strength of the right hand side, $\boldsymbol{u}$ is the velocity of the actin network (to be defined later), $\varepsilon$ is a length scale that defines the steepness of the diffuse interface, $G(\phi) = 18\phi^2(1 - \phi)^2$ is a double well potential with local minima at $\phi = 0$ and $\phi = 1$ (see [27, 28]), and $c = -\nabla \cdot (\nabla \phi / |\nabla \phi|)$ denotes the curvature of the membrane. The right hand side of Eq. (1) is $O(\varepsilon)$ and forces the field $\phi$ to maintain a hyperbolic tangent profile in the direction orthogonal to the cell's membrane. Essentially, Eq. (1) moves the cell's membrane with velocity $\boldsymbol{u}$, while maintaining a hyperbolic tangent profile. For a full understanding of Eq. (1), basic knowledge about the phase-field method is required [4, 51].

### 2.2. Cytosol biochemomechanics

The cytosolic machinery is described by the fields $\rho_f(\boldsymbol{x}, t)$, $\rho_g(\boldsymbol{x}, t)$, and $\rho_m(\boldsymbol{x}, t)$, which represent the density of actin filaments (F-actin), globular actin subunits (G-actin), and myosin II, respectively (see Fig. 1). The actin filament network, which plays a major role in amoeboid motion, is treated as a viscous fluid with velocity $\boldsymbol{u}(\boldsymbol{x}, t)$; see [28] for a rationale.

### 2.3. Myosin dynamics

In our model, myosin is transported by the actin network velocity and diffuses throughout the cell. The dynamics of $\rho_m$ are governed by the equation

$$\frac{\partial(\phi\rho_m)}{\partial t} + \nabla \cdot (\phi\rho_m\boldsymbol{u}) - \nabla \cdot \left[ D_m(\rho_f)\phi\nabla\rho_m \right] = 0. \tag{2}$$
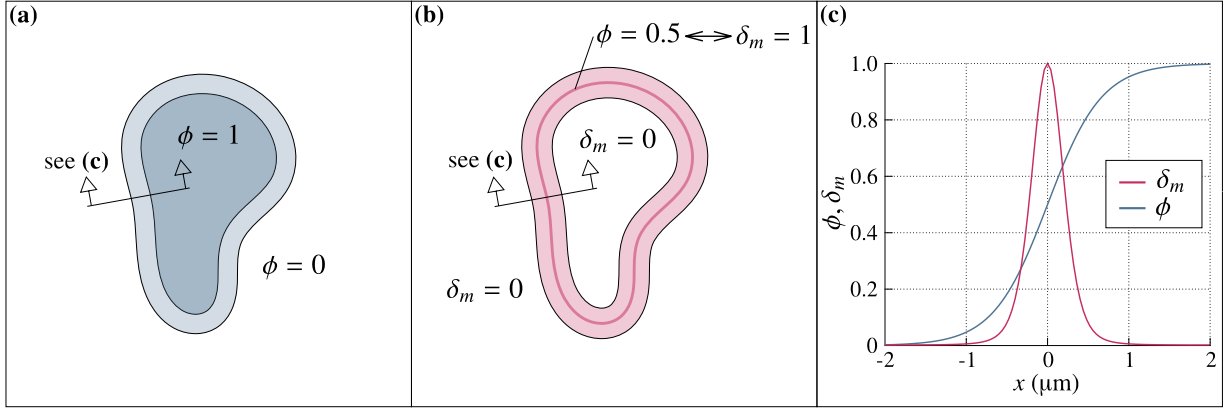
Figure 2: Conceptual description of the diffuse-domain framework used in the model. (a) The cell location is implicitly defined by the phase-field variable $\phi$. (b) The cell membrane marker $\delta_m$ is defined in terms of $\phi$. (c) $\phi$ and $\delta_m$ values across the membrane. The plot corresponds to $\varepsilon = 2\,\mu$m and $\varphi = 25$.

Here, $D_m(\rho_f) = D_{\max}/(1 + K^2\rho_f^2)$, where $D_{\max}$ and $K$ are constants. Note that $\rho_f$ will usually vary in space, producing a non-constant myosin diffusivity. Since $\rho_f$ tends to be lower at the back of the cell, $D_m$ will be higher there. This will produce an effective advection of myosin toward the back end of the cell, which is consistent with experimental evidence.

**Remark 1:** In practical computations, Eq. (2) will be solved with no-flux boundary conditions in a sufficiently large box denoted $\Omega$. The phase field $\phi : \Omega \mapsto \mathbb{R}$ will take a hyperbolic tangent profile, such that $\phi \approx 1$ in $\Omega_c \subset \Omega$ and $\phi \approx 0$ elsewhere, where $\Omega_c$ denotes the spatial region occupied by the cell. As we will show later, if suitable initial conditions are defined, this is approximately equivalent to solving the problem

$$\frac{\partial \rho_m}{\partial t} + \nabla \cdot (\rho_m \boldsymbol{u}) - \nabla \cdot \left[ D_m(\rho_f)\nabla\rho_m \right] = 0 \qquad \text{in} \quad \Omega_c, \tag{3}$$

$$\nabla\rho_m \cdot \boldsymbol{n}_{\Gamma_c} = 0 \qquad \text{on} \quad \Gamma_c, \tag{4}$$

where $\Gamma_c$ is the boundary of $\Omega_c$ and $\boldsymbol{n}_{\Gamma_c}$ is the unit outward normal to $\Gamma_c$. The advantage of Eq. (2) with respect to Eqs. (3) and (4) is that $\Omega$ is a fixed domain, while $\Omega_c$ is time dependent. This methodology is referred to as the diffuse-domain method in the phase-field community and will be used frequently throughout the paper. In simple words, the idea is to introduce the prefactor $\phi$ in the space and time derivatives as well as in the reaction terms to localize the equation to the cell's interior. The diffuse domain method shares features with immersed approaches; for further details see [55, 56].

*2.4. Actin dynamics*

Actin undergoes phase transformations between a globular (G-actin) and a filamentous state (F-actin). In addition, F-actin may be in the form of a passive structure or exhibit a protrusive behavior (see Fig. 1). To describe these two forms of F-actin we employ a bistable equation. Passive structures are associated to a stable homogeneous solution of the governing equation and protrusive structures to the other one. Protrusive structures are identified with areas of high F-actin concentration that represent pseudopods. We also know that the total amount of actin in the cell, that is,

$$\mathcal{N}[\rho_f, \rho_g] = \int_\Omega \phi(\rho_f + \rho_g)\mathrm{d}\Omega \tag{5}$$

must remain constant in time. Finally, actin phase transformations are controlled by the activator concentration that we call $a(\boldsymbol{x}, t)$. Higher values of $a$ favor the formation of F-actin protrusive structures (see Fig. 1). Taking this into account, we propose the energy functional

$$\mathcal{F}[\rho_f, \rho_g] = \int_\Omega \phi\left[ \frac{\varepsilon_f^2}{2}|\nabla\rho_f|^2 + \frac{\varepsilon_g^2}{2}|\nabla\rho_g|^2 + F\left(\rho_f, \rho_g, a\right) \right]\mathrm{d}\Omega + \frac{\alpha}{2}\left(\mathcal{N}_0 - \mathcal{N}\right)^2, \tag{6}$$
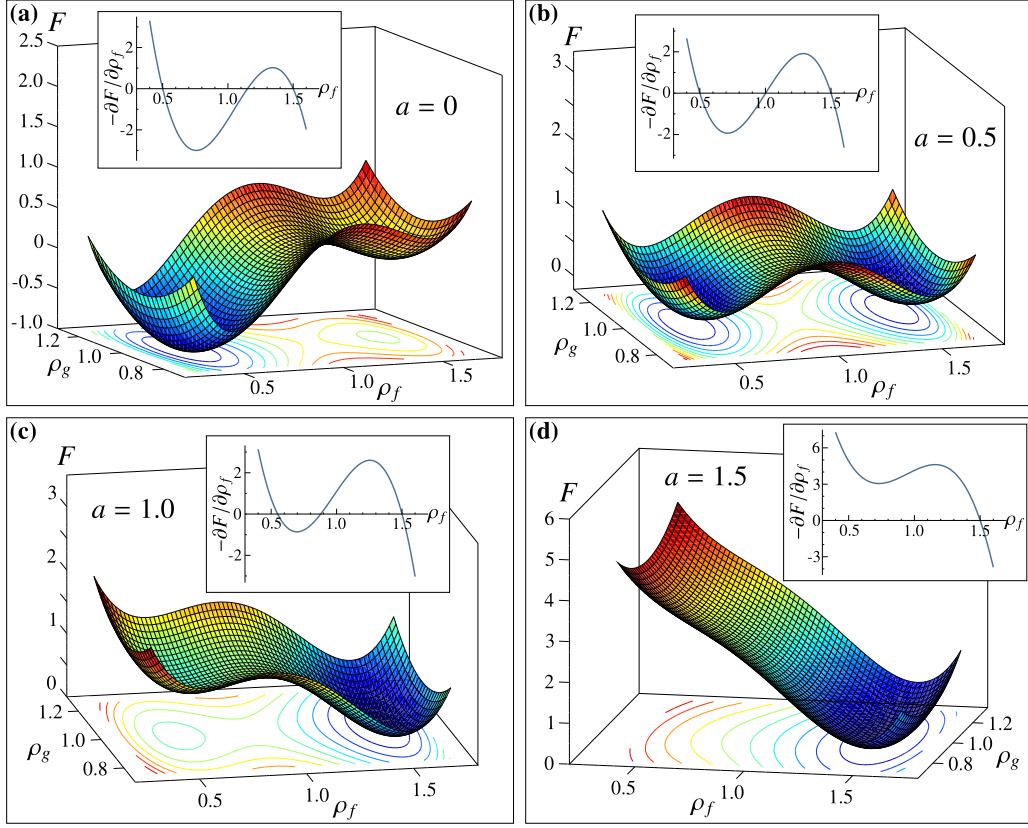
5

Figure 3: Actin free-energy functional: function $F$ and its derivative with respect to the F-actin density, depending on the activator concentration. (a) $a = 0$. (b) $a = 0.5$. (c) $a = 1.0$. (d) $a = 1.5$.

where $\varepsilon_f$ and $\varepsilon_g$ represent the diffusive length scales of $\rho_f$ and $\rho_g$, respectively. The quantity $\mathcal{N}_0$ denotes the total amount of actin at the initial time, that is, $\mathcal{N}_0 = \mathcal{N}[\rho_f(\cdot, 0), \rho_g(\cdot, 0)]$. Therefore, the last term of Eq. (6) energetically penalizes the variations of $\mathcal{N}$ with respect to time and $\alpha$ is a suitable penalty constant. The function $F$ controls actin phase transitions and is defined as

$$F\left(\rho_f, \rho_g, a\right) = 10(\rho_f - \rho_f^{\mathrm{pr}})^2(\rho_f - \rho_f^{\mathrm{pa}})^2 + 7.5(\rho_g - \rho_g^{\mathrm{eq}})^2 + I(a)(\rho_f - \rho_f^{\mathrm{pr}})^2[\rho_f + \beta(a)I(a)], \tag{7}$$

where $I(a) = a^2 - 2\exp(-4a)$ and $\beta(a) = 0.5[1 - (a - 1.8)^2/1.8^2]$. The constants $\rho_f^{\mathrm{pr}} = 3/2$, $\rho_f^{\mathrm{pa}} = 1/2$, and $\rho_g^{\mathrm{eq}} = 1$ represent, respectively, the F-actin concentration associated to protrusive and passive filamentous structures and the G-actin equilibrium concentration. Using the framework of non-conserved dynamics (standard in phase-field methods; see, e.g., [4]), we derive the evolution equations

$$\frac{\partial(\phi\rho_g)}{\partial t} + \nabla \cdot (\phi\rho_g \boldsymbol{u}) = -\Gamma_g \frac{\delta\mathcal{F}}{\delta\rho_g} = \Gamma_g\left[\varepsilon_g^2 \nabla \cdot (\phi\nabla\rho_g) - \phi\frac{\partial F}{\partial\rho_g} - \alpha\phi(\mathcal{N} - \mathcal{N}_0)\right], \tag{8}$$

$$\frac{\partial(\phi\rho_f)}{\partial t} + \nabla \cdot (\phi\rho_f \boldsymbol{u}) = -\Gamma_f \frac{\delta\mathcal{F}}{\delta\rho_f} = \Gamma_f\left[\varepsilon_f^2 \nabla \cdot (\phi\nabla\rho_f) - \phi\frac{\partial F}{\partial\rho_f} - \alpha\phi(\mathcal{N} - \mathcal{N}_0)\right], \tag{9}$$

where $\Gamma_f$ and $\Gamma_g$ are constants. $\delta\mathcal{F}/\delta\rho_f$ and $\delta\mathcal{F}/\delta\rho_g$ denote the variational derivatives of the functional $\mathcal{F}$ with respect to F-actin and G-actin density, respectively.

To gain insight into the dynamics of Eqs. (8) and (9), we show in Fig. 3 plots of $F$ for different values of the activator concentration. It may be observed that for a non-moving cell ($\boldsymbol{u} = 0$) with $\alpha = 0$, the homogeneous (constant

in space and time) solutions to Eqs. (8) and (9) are given by the local minima of $F$. Eq. (7) shows that $F$ is a convex function of $\rho_g$ for all values of $a$. The term $\frac{\partial F}{\partial \rho_g}$, which acts as a driving force in Eq. (8), vanishes at $\rho_g = \rho_g^{\text{eq}}$, which makes this homogeneous state an attractor of the solution. The dynamics of F-actin are more complex because the filaments can undergo phase transformations from a passive to a protrusive structure and vice versa depending on the value of the activator concentration. For sufficiently large values of the activator concentration [see Fig. 3(d)], $F$ is a convex function of $\rho_f$ with $\frac{\partial F}{\partial \rho_f}$ vanishing at $\rho_f = \rho_f^{\text{pr}}$. The homogeneous solution $\rho_f = \rho_f^{\text{pr}}$ is associated to protrusive structures which represent pseudopods. For lower values of $a$, however, $F$ may be a non-convex function of $\rho_f$ with $\frac{\partial F}{\partial \rho_f}$ vanishing at $\rho_f = \rho_f^{\text{pr}}$ and $\rho_f \approx \rho_f^{\text{pa}}$. The value $\rho_f \approx \rho_f^{\text{pa}}$ is associated to passive networks. Within the range of values of $a$ in which $F$ is a non-convex function of $\rho_f$, passive networks are energetically favored for lower values of $a$ [see Fig. 3(a)] and protrusive structures for larger values of $a$ [see Fig. 3(c)].

## 2.5. Actin flow

The actin filament network is treated as a viscous fluid governed by a Stokes-type equation. At the cellular scale the Reynolds number is very small and we can neglect the nonlinear convective term and inertial forces[1]. Following the rationale presented in [57] we also neglect the pressure term. Therefore, the governing equation is given by

$$\nabla \cdot (\boldsymbol{\sigma} + \boldsymbol{\sigma}_{\text{myo}} + \boldsymbol{\sigma}_{\text{prot}}) + \boldsymbol{F}_{\text{adh}} + \boldsymbol{F}_{\text{mem}} + \boldsymbol{F}_{\text{rep}} = 0, \tag{10}$$

where $\boldsymbol{\sigma}$, $\boldsymbol{\sigma}_{\text{myo}}$, and $\boldsymbol{\sigma}_{\text{prot}}$ are Cauchy stress tensors that define the rheology of the actin filament network. $\boldsymbol{F}_{\text{adh}}$, $\boldsymbol{F}_{\text{mem}}$, and $\boldsymbol{F}_{\text{rep}}$ are additional forces acting on the filament network. These include adhesion forces, the membrane forces, and repulsion forces created by rigid obstacles in the cell's path. These forces will be described later. Let us focus first on the rheology of the actin network.

### 2.5.1. Rheology of the actin network

The stress tensor

$$\boldsymbol{\sigma} = \phi[\mu(\nabla \boldsymbol{u} + \nabla \boldsymbol{u}^T) + \lambda(\nabla \cdot \boldsymbol{u})\boldsymbol{I}] \tag{11}$$

is the classical stress tensor of a Newtonian fluid with viscosity coefficients $\mu$ and $\lambda$. The prefactor $\phi$ is added to apply the diffuse domain method. The tensor $\boldsymbol{\sigma}_{\text{prot}}$ accounts for F-actin protrusive structures and is given by

$$\boldsymbol{\sigma}_{\text{prot}} = -\phi \rho_f \eta_f(\rho_f) \delta_f \nabla \phi \otimes \nabla \phi. \tag{12}$$

Here, $\phi$ is included again to use the diffuse domain method. The term $\rho_f \eta_f(\rho_f)$, where

$$\eta_f(\rho_f) = B\bar{\eta}_f + (1 - B)\bar{\eta}_f \mathcal{H}[\rho_f - (\rho_f^{\text{pr}} + \rho_f^{\text{pa}})/2], \tag{13}$$

controls the protrusive stress such that it is only significant for large values of $\rho_f$ (pseudopods). In Eq. (13), $B$ and $\bar{\eta}_f$ are constants, while $\mathcal{H}$ is a smoothed-out Heaviside function[2]. The term $\delta_f$ annihilates protrusive stresses in the vicinity of rigid obstacles. We take $\delta_f(\boldsymbol{x}) = \mathcal{H}(d_o(\boldsymbol{x}) - d_o^f)$ where $d_o(\boldsymbol{x})$ is the distance from the point $\boldsymbol{x}$ to the closest rigid obstacle and $d_o^f = 1.6\,\mu\text{m}$ represents an effective distance at which the presence of an obstacle starts to suppress protrusion forces. Since the normal to the cell's membrane $\boldsymbol{n}_{\Gamma_c}$ is parallel to $\nabla \phi$, it may be easily shown that the traction $\boldsymbol{\sigma}_{\text{prot}} \boldsymbol{n}_{\Gamma_c}$ is normal to the membrane. In addition, the term $\nabla \phi \otimes \nabla \phi$ localizes $\boldsymbol{\sigma}_{\text{prot}}$ to a neighborhood of the cell's membrane.

The tensor $\boldsymbol{\sigma}_{\text{myo}}$ accounts for the isotropic contractile stresses produced by myosin. We propose the expression

$$\boldsymbol{\sigma}_{\text{myo}} = \phi \rho_m \eta_m(\rho_m)\boldsymbol{I}, \tag{14}$$

where $\boldsymbol{I}$ is the identity tensor and $\eta_m(\rho_m) = A\bar{\eta}_m + (1 - A)\bar{\eta}_m \mathcal{H}(\rho_m - 0.9)$ is a function producing greater stress where myosin concentration is higher. The parameters $A$ and $\bar{\eta}_m$ play a similar role to $B$ and $\bar{\eta}_f$ in $\eta_f(\rho_f)$. Eq. (14) is a generalization to amoeboid motion of the model proposed in [28].

---

[1] Note that due to negligible inertia, cells have to permanently produce forces in order to move.

[2] Throughout this work, the smoothed-out Heaviside function is defined as $\mathcal{H}(x) = 0.5 + 0.5\tanh(7x)$. We use smooth approximations of the Heaviside function to increase the convergence rate of our Newton–Raphson algorithm.

### 2.5.2. Membrane, adhesion and contact forces

The term $F_{\mathrm{mem}}$ represents the forces exerted by the membrane. Our starting point to derive $F_{\mathrm{mem}}$ is the so-called Helfrich membrane energy [58, 59]. Let us define a closed surface $\Gamma_c$ that represents the cell's membrane. For vanishing spontaneous curvature, the Helfrich energy is defined as

$$\mathcal{F}_H(\Gamma_c) = \mathcal{F}_H^B(\Gamma_c) + \mathcal{F}_H^T(\Gamma_c), \tag{15}$$

where

$$\mathcal{F}_H^B(\Gamma_c) = \frac{K_c}{2} \int_{\Gamma_c} c^2 \mathrm{d}\Gamma \quad \text{and} \quad \mathcal{F}_H^T(\Gamma_c) = \gamma \int_{\Gamma_c} \mathrm{d}\Gamma. \tag{16}$$

Here, $K_c$ is the bending rigidity of the membrane, $c$ is the additive curvature of the surface, and $\gamma$ denotes the surface tension. Computing the membrane energy (and eventually membrane forces) using Eq. (16) requires an explicit tracking of the membrane. However, we wish to use a formulation consistent with that of the rest of the model and avoid any explicit interface tracking. To do so, we will use the phase-field method, describing $\Gamma_c$ by the level set $\phi = 1/2$. We will also use several properties of the phase-field method; see [4] for a rationale. One of the most useful properties of the phase-field method is that it allows to replace integrals on surfaces with integrals on volumes. For example, it may be shown that

$$\mathcal{F}_H^T(\Gamma_c) = \lim_{\varepsilon \to 0} \mathcal{F}_\varepsilon^T(\phi^\varepsilon). \tag{17}$$

Here,

$$\mathcal{F}_\varepsilon^T(\phi) = \gamma \int_\Omega \left( \frac{G(\phi)}{\varepsilon} + \frac{\varepsilon}{2} |\nabla \phi|^2 \right) \mathrm{d}\Omega \tag{18}$$

and $\phi^\varepsilon(\boldsymbol{x}) = \tanh(d_{\Gamma_c}(\boldsymbol{x})/\varepsilon)$, where $d_{\Gamma_c}(\boldsymbol{x})$ is a scaled distance from the point $\boldsymbol{x}$ to the surface $\Gamma_c$ and $\Omega$ is a sufficiently large subset of $\mathbb{R}^3$ which may be associated to our computational domain. The advantage of the functional $\mathcal{F}_\varepsilon^T$ with respect to $\mathcal{F}_H^T$ is that the integral in $\mathcal{F}_\varepsilon^T$ is defined on a known and fixed domain. We will also make use of an important property of phase fields referred to as *equipartition of energy* [60], that is,

$$G(\phi^\varepsilon) - \frac{\varepsilon^2}{2} |\nabla \phi^\varepsilon|^2 \to 0 \quad \text{as} \quad \varepsilon \to 0. \tag{19}$$

The equipartition property allows us to find alternative expression for $\mathcal{F}_\varepsilon^T$. For example, we know that

$$\mathcal{F}_\varepsilon^T(\phi) \to \gamma \int_\Omega \varepsilon |\nabla \phi|^2 \mathrm{d}\Omega \quad \text{as} \quad \varepsilon \to 0 \tag{20}$$

if $\phi$ is of the form of $\phi^\varepsilon$, which is guaranteed because Eq. (1) produces solutions with a hyperbolic tangent profile. We can also express the additive curvature of $\Gamma_c$, namely $c$, implicitly in terms of the phase field $\phi$. From basic differential geometry, we know

$$c = \nabla_{\Gamma_c} \cdot \boldsymbol{n}_{\Gamma_c}, \tag{21}$$

where $\nabla_{\Gamma_c} \cdot$ denotes the divergence operator on the surface $\Gamma_c$. The vector $\boldsymbol{n}_{\Gamma_c}$ can be expressed in terms of the phase field as $\boldsymbol{n}_{\Gamma_c} = -\nabla \phi / |\nabla \phi|$ and standard identities of differential geometry may be used to show that

$$c = -\frac{1}{|\nabla \phi|} \left( \nabla^2 \phi - \frac{1}{2|\nabla \phi|^2} \nabla \phi \cdot \nabla(|\nabla \phi|^2) \right). \tag{22}$$

Utilizing the property of equipartition of energy, this can be simplified to

$$c \approx -\frac{1}{|\nabla \phi|} \left( \nabla^2 \phi - \frac{1}{\varepsilon^2} G'(\phi) \right). \tag{23}$$

Using Eqs. (20) and (23), it may be shown that

$$\mathcal{F}_H^B(\Gamma_c) \approx \mathcal{F}_\varepsilon^B(\phi) = \frac{K_c}{2} \int_\Omega \varepsilon \left( \nabla^2 \phi - \frac{1}{\varepsilon^2} G'(\phi) \right)^2 \mathrm{d}\Omega. \tag{24}$$

From Eq. (18), we conclude that

$$\mathcal{F}_H^T(\Gamma_c) \approx \mathcal{F}_\varepsilon^T(\phi) = \gamma \int_\Omega \left( \frac{G(\phi)}{\varepsilon} + \frac{\varepsilon}{2}|\nabla\phi|^2 \right) d\Omega. \tag{25}$$

Defining $\mathcal{F}_\varepsilon(\phi) = \mathcal{F}_\varepsilon^T(\phi) + \mathcal{F}_\varepsilon^B(\phi) \approx \mathcal{F}_H(\Gamma_c)$, the membrane forces per unit volume may be computed as

$$\boldsymbol{F}_{\text{mem}} = -\frac{\delta\mathcal{F}_\varepsilon(\phi)}{\delta\Gamma_c}, \tag{26}$$

where $\frac{\delta\mathcal{F}_\varepsilon(\phi)}{\delta\Gamma_c}$ denotes the variational derivative of $\mathcal{F}_\varepsilon(\phi)$ with respect to variations of the surface $\Gamma_c$ in its normal direction. This may be also expressed as

$$\boldsymbol{F}_{\text{mem}} = \frac{\delta\mathcal{F}_\varepsilon(\phi)}{\delta\phi}\nabla\phi. \tag{27}$$

Membrane forces can be split as $\boldsymbol{F}_{\text{mem}} = \boldsymbol{F}_{\text{bend}} + \boldsymbol{F}_{\text{ten}}$ where

$$\boldsymbol{F}_{\text{bend}} = \frac{\delta\mathcal{F}_\varepsilon^B(\phi)}{\delta\phi}\nabla\phi = K_c\varepsilon\nabla\phi\left[\nabla^2\left(\nabla^2\phi - \frac{G'(\phi)}{\varepsilon^2}\right) - \frac{G''(\phi)}{\varepsilon^2}\left(\nabla^2\phi - \frac{G'(\phi)}{\varepsilon^2}\right)\right], \tag{28}$$

$$\boldsymbol{F}_{\text{ten}} = \frac{\delta\mathcal{F}_\varepsilon^T(\phi)}{\delta\phi}\nabla\phi = \gamma\nabla\phi\left(\frac{G'(\phi)}{\varepsilon} - \varepsilon\nabla^2\phi\right). \tag{29}$$

It may be easily shown that $\boldsymbol{F}_{\text{ten}}$ is a force orthogonal to the cell's membrane and proportional to its curvature.

Once we have derived membrane forces, we focus on adhesion and contact forces. The force $\boldsymbol{F}_{\text{adh}} = -\varsigma\boldsymbol{u}$ models a hydrodynamic drag[3]. The force $\boldsymbol{F}_{\text{rep}}$ models repulsive contact forces produced by rigid solid obstacles in the cell's path. It may be expressed as

$$\boldsymbol{F}_{\text{rep}} = \nabla \cdot \boldsymbol{\sigma}_{\text{rep}} = \nabla \cdot (\phi\eta_{\text{rep}}\delta_{\text{rep}}\nabla\phi \otimes \nabla\phi), \tag{30}$$

where $\eta_{\text{rep}}$ is a constant and $\delta_{\text{rep}}$ is a function that depends on the position and acts as a localizer of obstacles. We take

$$\delta_{\text{rep}} = \mathcal{H}(d_o^{\text{ef}} - d_o(\boldsymbol{x})), \tag{31}$$

where $d_o(\boldsymbol{x})$ is the distance between the point $\boldsymbol{x}$ and the closest obstacle and $d_o^{\text{ef}}$ is a small constant that represents an effective distance at which the cells feel an obstacle. In the computations we took $d_o^{\text{ef}} = 0.7\,\mu\text{m}$. It can be easily shown that $\boldsymbol{F}_{\text{rep}}$ is a force normal to the membrane and pointing towards the interior of the cell.

## 2.6. Activator dynamics

The growth of pseudopods is controlled by membrane signaling molecules (e.g., PIP3 [3]), which trigger actin nucleation. We model the membrane signaling dynamics by using a single membrane-located compound that we call activator $a(\boldsymbol{x}, t)$. We make use of the diffuse domain method to localize the activator dynamics to the membrane without resorting to surface PDEs [55]. This is accomplished by using the smooth membrane marker

$$\delta_m(\phi) = \exp[-\varphi(\phi - 0.5)^2], \tag{32}$$

which has been plotted in Fig. 2. The constant parameter $\varphi$ defines the thickness of the marker. Our model for the activator dynamics is given by the equation

$$\frac{\partial(\delta_m a)}{\partial t} + \nabla \cdot (\delta_m a\boldsymbol{u}) = \nabla \cdot (D_a\delta_m\nabla a) - r_a\delta_m a + b_a\delta_m S_a, \tag{33}$$

which accounts for the advective transport, diffusion throughout the membrane (with diffusion constant $D_a$), a natural decay (with rate $r_a$), and a growth term $S_a$ whose strength is controlled by the parameter $b_a$. A fundamental model of the term $S_a$ requires knowledge about the mechanisms that control the autocatalysis of membrane-bound activators. Since these mechanisms are not well understood [61], we resort to experimental data [62]. These data consist of several probability distribution functions that control the position and time at which the activator triggers actin
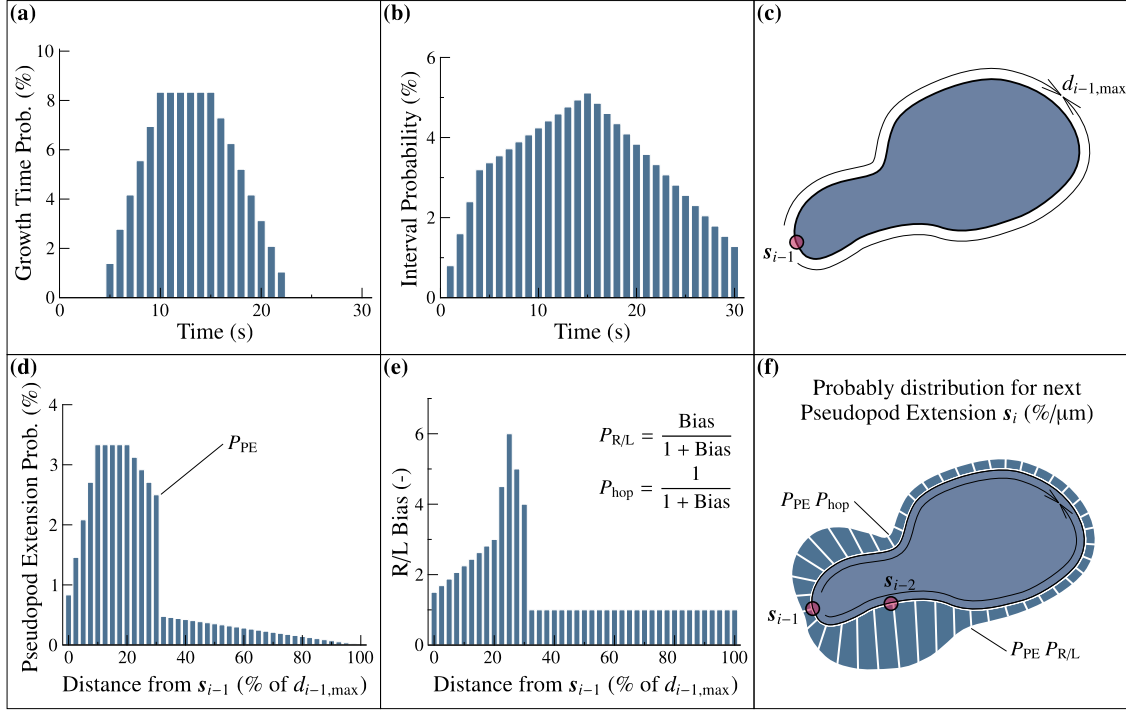
Figure 4: Determination of pseudopod formation. The probability distributions are derived from [62]. (a) Pseudopod growth time probability. (b) Pseudopod interval time distribution. (c) Perimeter distance from previous source. (d) Probability distribution for next pseudopod location in terms of the perimeter distance. (e) Right/left bias function. (f) Probability distribution for next pseudopod extension.

nucleation. For simplicity, we initially describe this procedure in a 2D scenario. The probability distributions (see Fig. 4) are used to define $S_a$, which creates peaks in the activator concentration at certain points in space and time. In particular, we take $S_a = (a_{max} - a) \sum_i \delta_{x,i} \delta_{t,i}$ that drives $a$ to $a_{max}$ at certain time intervals ($\delta_{t,i}$) and spatial areas ($\delta_{x,i}$) of the membrane. To define the temporal localizers we make use of the *interval* and the *growth time*. The interval $\Delta\tau_i$ represents the period of time between the extension of two consecutive pseudopods. Therefore we can define the set of times $\{\tau_{0,1}, \tau_{0,2}, ...\}$, where $\tau_{0,1} = 0$ and $\tau_{0,i} = \tau_{0,i-1} + \Delta\tau_i$, such that $\tau_{0,i}$ indicates the time at which the activator peak $i$ is switched on. Each peak will be active during a growth time $\Delta T_i$. Thus, the temporal localizer is defined by $\delta_{t,i} = \mathcal{H}(\Delta T_i - (t - \tau_{0,i}))$. The growth time ($\Delta T_i$) and the interval ($\Delta\tau_i$) are two random variables given by the probability functions plotted in Figs. 4(a) and (b), respectively. Note that there may be none, one, or more than one active sources at the same time. The spatial location is given by the function $\delta_{x,i} = \mathcal{H}(r_p - d_i(x))$, where $d_i$ represents the distance to the center of the activator source $i$ ($s_i$) and $r_p$ is its approximate radius. In the case of a two-dimensional problem, the location of $s_i$ is derived from the probability function plotted in Fig. 4(f) that depends on the location of the two previous sources ($s_{i-1}$ and $s_{i-2}$). To establish the location of a new peak ($s_i$), we need to define the probability distribution along the membrane using the functions in Figs. 4(d) and (e). The probability function will be $P_{PE} P_{R/L}$ on the side of the membrane where $s_{i-2}$ is located, and $P_{PE} P_{hop}$ on the other side of the membrane. Note that each source moves together with the membrane and therefore, the probability distribution in Fig. 4(f) changes over time. In addition, the cell-obstacle contact impedes pseudopod formation [63] modifying the probability function such that $P_{PE}(x) = 0$ if $d_o(x) < 1.3\,\mu m$. In summary, each time a new peak emerges, we select three random values using the probability distributions shown in Fig. 4. These quantities represent growth time (time during which the peak is active), interval (permits to compute the time at which the next peak will arise), and location of pseudopod extension.

The extension of this procedure to 3D problems is not straightforward, primarily due to the absence of experi-

---

[3]In a two-dimensional simulation that represents cell motion on a planar substrate, this force may be interpreted as a friction force between the cell and the underlying substrate. In the biological problem, this force is accomplished by the transmembrane protein family called integrin.

mental data in three dimensions. To avoid computing the probability distribution over the entire cell surface, in the case of a 3D calculation, we proceed as follows: We compute the growth time and the interval as before. Then, we determine the distance between $s_{i-1}$ and each point of the cell's surface following the shortest path contained in the membrane. From this computation, we obtain $d_{i-1,\max}$ as shown in Fig. 4(c) for the 2D case. Once we have $d_{i-1,\max}$, we generate a random number using the probability distribution in Fig. 4(d). This number represents the actual value of the distance between $s_{i-1}$ and $s_i$ that we call $d_{i-1}^i$. We can now enter in Fig. 4(e) with $d_{i-1}^i$ and obtain $P_{R/L}$ and $P_{hop}$. Knowing the probabilities of the cell to alternate left and right ($P_{R/L}$) or to hop ($P_{hop}$), we can use a random number generator to determine if the cell will alternate left and right or hop. Then, we can compute the locus of the points of the membrane that are located at a distance $d_{i-1}^i$ of $s_{i-1}$. The locus of these points is one (or several) curve(s) that we denote by $l_{d_{i-1}^i}$. The source activator $s_i$ will be located on the curve(s) $l_{d_{i-1}^i}$. The next step is to compute two points of $l_{d_{i-1}^i}$, namely $C_i$ and $D_i$. The point $C_i$ (respectively, $D_i$) is the closest (respectively, the farthest) point of $l_{d_{i-1}^i}$ to $s_{i-2}$. If the cell is to alternate left and right (respectively, hop) the location of $s_i$ will be determined by a normal probability distribution that is centered at $C_i$ (respectively, $D_i$).

## 2.7. Continuous problem in strong form

Let $\Omega \subset \mathbb{R}^{d_s}$ be an open set that represents our computational domain. Unless otherwise stated, $\Omega$ is simply a box sufficiently large to enclose the cell. Let $\Gamma$ be the boundary of $\Omega$, assumed sufficiently smooth. The strong form of the problem can be stated as: Given a time interval of interest $[0, T]$ and suitable initial and boundary conditions, find $\phi : \overline{\Omega} \times (0, T) \to \mathbb{R}$, $\rho_m : \overline{\Omega} \times (0, T) \to \mathbb{R}$, $\rho_f : \overline{\Omega} \times (0, T) \to \mathbb{R}$, $\rho_g : \overline{\Omega} \times (0, T) \to \mathbb{R}$, $a : \overline{\Omega} \times (0, T) \to \mathbb{R}$, and $\boldsymbol{u} : \overline{\Omega} \times (0, T) \to \mathbb{R}^{d_s}$ such that

$$\frac{\partial \phi}{\partial t} + \boldsymbol{u} \cdot \nabla \phi = \Gamma_\phi \left( \varepsilon \nabla^2 \phi - \frac{G'(\phi)}{\varepsilon} + c\varepsilon |\nabla \phi| \right) \qquad \text{in} \quad \Omega \times (0, T), \tag{34.1}$$

$$\frac{\partial (\phi \rho_m)}{\partial t} + \nabla \cdot (\phi \rho_m \boldsymbol{u}) = \nabla \cdot \left[ D_m(\rho_f) \phi \nabla \rho_m \right] \qquad \text{in} \quad \Omega \times (0, T), \tag{34.2}$$

$$\frac{\partial (\phi \rho_f)}{\partial t} + \nabla \cdot (\phi \rho_f \boldsymbol{u}) = \Gamma_f \left[ \varepsilon_f^2 \nabla \cdot (\phi \nabla \rho_f) - \phi \frac{\partial F}{\partial \rho_f} - \alpha \phi (\mathcal{N} - \mathcal{N}_0) \right] \qquad \text{in} \quad \Omega \times (0, T), \tag{34.3}$$

$$\frac{\partial (\phi \rho_g)}{\partial t} + \nabla \cdot (\phi \rho_g \boldsymbol{u}) = \Gamma_g \left[ \varepsilon_g^2 \nabla \cdot (\phi \nabla \rho_g) - \phi \frac{\partial F}{\partial \rho_g} - \alpha \phi (\mathcal{N} - \mathcal{N}_0) \right] \qquad \text{in} \quad \Omega \times (0, T), \tag{34.4}$$

$$\frac{\partial (\delta_m a)}{\partial t} + \nabla \cdot (\delta_m a \boldsymbol{u}) = \nabla \cdot (D_a \delta_m \nabla a) - r_a \delta_m a + b_a \delta_m S_a \qquad \text{in} \quad \Omega \times (0, T), \tag{34.5}$$

$$\nabla \cdot (\boldsymbol{\sigma} + \boldsymbol{\sigma}_{myo} + \boldsymbol{\sigma}_{prot}) + \boldsymbol{F}_{adh} + \boldsymbol{F}_{mem} + \boldsymbol{F}_{rep} = 0 \qquad \text{in} \quad \Omega \times (0, T). \tag{34.6}$$

# 3. Numerical formulation

## 3.1. Continuous problem in weak form

Let $\mathcal{S} = \left\{ \phi \mid \phi(\cdot, t) \in \mathcal{H}^3(\Omega) \right\}$ be the trial solution space. Here, $\mathcal{H}^3(\Omega)$ denotes the Sobolev space of square-integrable functions with square-integrable first, second, and third derivatives. Analogously, we define a weighting function space $\mathcal{V} = \left\{ w \mid w \in \mathcal{H}^3(\Omega) \right\}$.

We derive a weak form of Eqs. (34.1)–(34.6) by multiplying them with weighting functions and integrating by parts repeatedly. We work under the assumptions of periodic boundary conditions and sufficient regularity. Let $(\cdot, \cdot)_\Omega$ denote the $\mathcal{L}^2$ inner product with respect to the domain $\Omega$. We call $n_{dof} = 5 + d_s$ the number of scalar unknowns. Thus, the problem can be stated as: Find $\boldsymbol{U} = \{\phi, \rho_m, \rho_f, \rho_g, a, \boldsymbol{u}\} \in \mathcal{S}^{n_{dof}}$ such that for all $\boldsymbol{W} = \{p, q, r, s, v, \boldsymbol{w}\} \in \mathcal{V}^{n_{dof}}$

$$\mathcal{B}(\boldsymbol{W}, \boldsymbol{U}) = 0 \tag{35}$$

with

$$
\begin{aligned}
\mathcal{B}(\boldsymbol{W}, \boldsymbol{U}) =\ & \left(p, \frac{\partial \phi}{\partial t}\right)_{\Omega} + \left(q, \phi \frac{\partial \rho_m}{\partial t}\right)_{\Omega} + \left(q, \rho_m \frac{\partial \phi}{\partial t}\right)_{\Omega} + \left(r, \phi \frac{\partial \rho_f}{\partial t}\right)_{\Omega} + \left(r, \rho_f \frac{\partial \phi}{\partial t}\right)_{\Omega} + \left(s, \phi \frac{\partial \rho_g}{\partial t}\right)_{\Omega} + \left(s, \rho_g \frac{\partial \phi}{\partial t}\right)_{\Omega} \\
& + \left(v, \delta_m \frac{\partial a}{\partial t}\right)_{\Omega} + \left(v, a\delta_m' \frac{\partial \phi}{\partial t}\right)_{\Omega} + \left(p, \boldsymbol{u} \cdot \nabla \phi\right)_{\Omega} + \left(\nabla p, \Gamma_{\phi} \varepsilon \nabla \phi\right)_{\Omega} + \left(p, \Gamma_{\phi} \frac{G'}{\varepsilon}\right)_{\Omega} - \left(\nabla p, \Gamma_{\phi} \varepsilon \nabla \phi\right)_{\Omega} \\
& - \left(p, \frac{\Gamma_{\phi}\varepsilon}{|\nabla \phi|} \nabla \phi \cdot \nabla(|\nabla \phi|)\right)_{\Omega} - \left(\nabla q, \phi \rho_m \boldsymbol{u}\right)_{\Omega} + \left(\nabla q, D_m \phi \nabla \rho_m\right)_{\Omega} - \left(\nabla r, \phi \rho_f \boldsymbol{u}\right)_{\Omega} + \left(\nabla r, \Gamma_f \varepsilon_f^2 \phi \nabla \rho_f\right)_{\Omega} \\
& + \left(r, \Gamma_f \phi \frac{\partial F}{\partial \rho_f}\right)_{\Omega} + \left(r, \Gamma_f \alpha \phi(\mathcal{N} - \mathcal{N}_0)\right)_{\Omega} - \left(\nabla s, \phi \rho_g \boldsymbol{u}\right)_{\Omega} + \left(\nabla s, \Gamma_g \varepsilon_g^2 \phi \nabla \rho_g\right)_{\Omega} + \left(s, \Gamma_g \phi \frac{\partial F}{\partial \rho_g}\right)_{\Omega} \\
& + \left(s, \Gamma_g \alpha \phi(\mathcal{N} - \mathcal{N}_0)\right)_{\Omega} - \left(\nabla v, \delta_m a \boldsymbol{u}\right)_{\Omega} + \left(\nabla v, D_a \delta_m \nabla a\right)_{\Omega} + \left(v, r_a \delta_m a\right)_{\Omega} - \left(v, b_a \delta_m S_a\right)_{\Omega} \\
& - \left(\nabla \boldsymbol{w}, \phi \left[\mu(\nabla \boldsymbol{u} + \nabla \boldsymbol{u}^T) + \lambda(\nabla \cdot \boldsymbol{u})\boldsymbol{I}\right]\right)_{\Omega} - \left(\nabla \boldsymbol{w}, \phi \rho_m \eta_m \boldsymbol{I}\right)_{\Omega} + \left(\nabla \boldsymbol{w}, \phi \rho_f \eta_f \delta_f \nabla \phi \otimes \nabla \phi\right)_{\Omega} \\
& - \left(\boldsymbol{w}, \varsigma \boldsymbol{u}\right)_{\Omega} - \left(\boldsymbol{w}, \gamma \left(\varepsilon \nabla^2 \phi - \frac{G'}{\varepsilon}\right) \nabla \phi\right)_{\Omega} - \left(\nabla(\boldsymbol{w} \cdot \nabla \phi), K_c \varepsilon \nabla(\nabla^2 \phi)\right)_{\Omega} + \left(\nabla(\boldsymbol{w} \cdot \nabla \phi), \frac{K_c}{\varepsilon} G'' \nabla \phi\right)_{\Omega} \\
& - \left(\boldsymbol{w}, \frac{K_c}{\varepsilon} G'' \nabla^2 \phi \nabla \phi\right)_{\Omega} + \left(\boldsymbol{w}, \frac{K_c}{\varepsilon^3} G' G'' \nabla \phi\right)_{\Omega} - \left(\nabla \boldsymbol{w}, \phi \eta_{\mathrm{rep}} \delta_{\mathrm{rep}} \nabla \phi \otimes \nabla \phi\right)_{\Omega}.
\end{aligned}
\tag{36}
$$

### 3.2. Semidiscrete formulation

The discretization of Eqs. (35) and (36) cannot be done using classical finite elements because the discrete trial and weight function spaces need to be a subset of $\mathcal{H}^3(\Omega)$; otherwise the integrals in (36) are not well defined. Classical finite element spaces spanned by basis functions which are $C^0$-continuous across element boundaries do not permit to generate discrete spaces contained in $\mathcal{H}^3$. To overcome this limitation, we make use of isogeometric analysis (IGA) [64, 65], which is a generalization of the finite element method that aims at unifying design and analysis. IGA uses B-splines or non-uniform B-splines (NURBS) to define the discrete spaces. B-splines and NURBS have controllable global continuity which permits to define discrete spaces that are subsets of $\mathcal{H}^3(\Omega)$. The discretization of Eqs. (35) and (36) requires the use of at least cubic splines with $C^2$-global continuity. These functions can be easily generated as shown in [66]. Let us call $\mathcal{S}^h$ and $\mathcal{V}^h$ the trial and weighting function discrete spaces, which are assumed to be identical. The spline basis functions are generically denoted by $N_A$ so that $\mathcal{S}^h = \mathcal{V}^h = \mathrm{span}\{N_A\}_{A=1}^{n_b}$, where $n_b$ is the dimension of the discrete space.

The discrete problem can be stated as: Find $\boldsymbol{U}^h = \{\phi^h, \rho_m^h, \rho_f^h, \rho_g^h, a^h, \boldsymbol{u}^h\} \in (\mathcal{S}^h)^{n_{\mathrm{dof}}}$ such that for all $\boldsymbol{W}^h = \{p^h, q^h, r^h, s^h, v^h, \boldsymbol{w}^h\} \in (\mathcal{V}^h)^{n_{\mathrm{dof}}}$

$$
\mathcal{B}(\boldsymbol{W}^h, \boldsymbol{U}^h) = 0
\tag{37}
$$

where

$$
\phi^h(\boldsymbol{x}, t) = \sum_{A=1}^{n_b} \phi_A(t) N_A(\boldsymbol{x}), \qquad p^h(\boldsymbol{x}) = \sum_{A=1}^{n_b} p_A N_A(\boldsymbol{x}).
\tag{38}
$$

The rest of the variables in $\boldsymbol{U}^h$ and $\boldsymbol{W}^h$ are defined analogously.

**Remark 2:** In Section 4.2.1 we will show that the bending resistance of the membrane is negligible with respect to the acting forces. In all sections other than 4.2.1 our computations do not include the bending energy and, therefore, the discrete space needs to be $\mathcal{H}^2$-conforming only. In this case, employing quadratic NURBS basis functions, which are globally $C^1$-continuous, the Galerkin form is well defined and the computations are usually faster in our implementation[4]

---

[4]$C^2$-continuous cubic functions are slower than $C^1$ quadratics due to the use of sub-optimal element-based Gaussian quadrature in our implementation. Alternative quadratures and/or assembly methods can be used that speed up the computations dramatically [67]. Another alternative is to use collocation methods [68]. An important feature of IGA that was recently noticed is that it is possible to define collocation points that render the Galerkin solution exactly [69].

## 3.3. Time discretization and numerical implementation

At this stage, our formulation remains continuous in time. Here, we describe our time-stepping scheme, which is based on the generalized-$\alpha$ method. The generalized-$\alpha$ method was originally derived in [70] for the equations of structural dynamics and subsequently applied to turbulence computations [71] and to the Cahn–Hilliard phase-field model in [72].

### 3.3.1. Time stepping scheme

To illustrate our method, let us divide the time interval of interest $[0, T]$ into a sequence of subintervals $(t_n, t_{n+1})$ with fixed time-step size $\Delta t = t_{n+1} - t_n$. We define the following residual vectors

$$\boldsymbol{R}^\Phi = \left\{R_A^\Phi\right\}, \qquad \boldsymbol{R}^M = \left\{R_A^M\right\}, \qquad \boldsymbol{R}^F = \left\{R_A^F\right\}, \qquad \boldsymbol{R}^G = \left\{R_A^G\right\}, \qquad \boldsymbol{R}^A = \left\{R_A^A\right\}, \qquad \boldsymbol{R}^U = \left\{R_{A,j}^U\right\}. \tag{39}$$

Here, $A \in \{1, \ldots, n_b\}$ is a control-variable index, and $j$ is a dimension index which runs from 1 to $d_s$. The components of the residual vector are given by

$$R_A^\Phi = \mathcal{B}\left(\{N_A, 0, 0, 0, 0, 0\}, \{\phi^h, \rho_m^h, \rho_f^h, \rho_g^h, a^h, \boldsymbol{u}^h\}\right), \tag{40.1}$$

$$R_A^M = \mathcal{B}\left(\{0, N_A, 0, 0, 0, 0\}, \{\phi^h, \rho_m^h, \rho_f^h, \rho_g^h, a^h, \boldsymbol{u}^h\}\right), \tag{40.2}$$

$$R_A^F = \mathcal{B}\left(\{0, 0, N_A, 0, 0, 0\}, \{\phi^h, \rho_m^h, \rho_f^h, \rho_g^h, a^h, \boldsymbol{u}^h\}\right), \tag{40.3}$$

$$R_A^G = \mathcal{B}\left(\{0, 0, 0, N_A, 0, 0\}, \{\phi^h, \rho_m^h, \rho_f^h, \rho_g^h, a^h, \boldsymbol{u}^h\}\right), \tag{40.4}$$

$$R_A^A = \mathcal{B}\left(\{0, 0, 0, 0, N_A, 0\}, \{\phi^h, \rho_m^h, \rho_f^h, \rho_g^h, a^h, \boldsymbol{u}^h\}\right), \tag{40.5}$$

$$R_{A,j}^U = \mathcal{B}\left(\{0, 0, 0, 0, 0, N_A\boldsymbol{e}_j\}, \{\phi^h, \rho_m^h, \rho_f^h, \rho_g^h, a^h, \boldsymbol{u}^h\}\right), \tag{40.6}$$

where $\boldsymbol{e}_j$ denotes the $j$-th unit vector of the Cartesian basis. Let us call $\boldsymbol{V}$ and $\dot{\boldsymbol{V}}$ the global vector of control variables of the degrees of freedom and its time derivative. Let us denote $\boldsymbol{V}_n$ and $\dot{\boldsymbol{V}}_n$ the time-discrete approximations of $\boldsymbol{V}$ and $\dot{\boldsymbol{V}}$ at time $t_n$. Using this notation, our time-integration algorithm may be defined as follows: Given $\dot{\boldsymbol{V}}_n$, $\boldsymbol{V}_n$, and $\Delta t$, find $\dot{\boldsymbol{V}}_{n+1}$, $\boldsymbol{V}_{n+1}$, $\dot{\boldsymbol{V}}_{n+\alpha_m}$, and $\boldsymbol{V}_{n+\alpha_f}$ such that

$$\boldsymbol{R}^\Phi\left(\dot{\boldsymbol{V}}_{n+\alpha_m}, \boldsymbol{V}_{n+\alpha_f}\right) = 0, \tag{41.1}$$

$$\boldsymbol{R}^M\left(\dot{\boldsymbol{V}}_{n+\alpha_m}, \boldsymbol{V}_{n+\alpha_f}\right) = 0, \tag{41.2}$$

$$\boldsymbol{R}^F\left(\dot{\boldsymbol{V}}_{n+\alpha_m}, \boldsymbol{V}_{n+\alpha_f}\right) = 0, \tag{41.3}$$

$$\boldsymbol{R}^G\left(\dot{\boldsymbol{V}}_{n+\alpha_m}, \boldsymbol{V}_{n+\alpha_f}\right) = 0, \tag{41.4}$$

$$\boldsymbol{R}^A\left(\dot{\boldsymbol{V}}_{n+\alpha_m}, \boldsymbol{V}_{n+\alpha_f}\right) = 0, \tag{41.5}$$

$$\boldsymbol{R}^U\left(\dot{\boldsymbol{V}}_{n+\alpha_m}, \boldsymbol{V}_{n+\alpha_f}\right) = 0, \tag{41.6}$$

$$\dot{\boldsymbol{V}}_{n+\alpha_m} = \dot{\boldsymbol{V}}_n + \alpha_m\left(\dot{\boldsymbol{V}}_{n+1} - \dot{\boldsymbol{V}}_n\right), \tag{41.7}$$

$$\boldsymbol{V}_{n+\alpha_f} = \boldsymbol{V}_n + \alpha_f\left(\boldsymbol{V}_{n+1} - \boldsymbol{V}_n\right), \tag{41.8}$$

$$\boldsymbol{V}_{n+1} = \boldsymbol{V}_n + \Delta t\dot{\boldsymbol{V}}_n + \chi\Delta t\left(\dot{\boldsymbol{V}}_{n+1} - \dot{\boldsymbol{V}}_n\right), \tag{41.9}$$

where $\alpha_m$, $\alpha_f$, and $\chi$ are real-valued parameters that define the method. These parameters are selected based on considerations of accuracy and stability. Jansen et al. [71] proved that, for a model problem, second-order accuracy in time is achieved if

$$\chi = \frac{1}{2} + \alpha_m - \alpha_f, \tag{42}$$

while unconditional stability is attained if

$$\alpha_m \geq \alpha_f \geq \frac{1}{2}. \tag{43}$$

The method parameters can be expressed in terms of $\varrho_\infty$, the spectral radius of the amplification matrix as $\Delta t \to \infty$, by way of the relations

$$\alpha_m = \frac{1}{2}\left(\frac{3 - \varrho_\infty}{1 + \varrho_\infty}\right), \tag{44}$$

$$\alpha_f = \frac{1}{1 + \varrho_\infty}. \tag{45}$$

Setting $\chi$ according to Eq. (42), a family of second-order accurate and unconditionally $A$-stable time integration schemes is defined in terms of the parameter $\varrho_\infty \in [0, 1]$. The value $\varrho_\infty = 0.5$ has proved an effective choice for turbulence computations and for the Cahn–Hilliard phase-field model [72]. We adopt this value for all the simulations presented in this paper.

The nonlinear system of equations (41) is approximated by using Newton–Raphson's method. Our initial guesses for the control variables at time $t_{n+1}$ are:

$$\boldsymbol{V}_{n+1,(0)} = \boldsymbol{V}_n, \tag{46}$$

$$\dot{\boldsymbol{V}}_{n+1,(0)} = \frac{\chi - 1}{\chi}\dot{\boldsymbol{V}}_n. \tag{47}$$

Then, we perform the nonlinear iterations by repeating the following steps for $i = 1, 2, \cdots, i_{\max}$, or until convergence is achieved:

1. Evaluate the global unknowns at intermediate time levels

$$\boldsymbol{V}_{n+\alpha_f,(i)} = \boldsymbol{V}_n + \alpha_f\left(\boldsymbol{V}_{n+1,(i-1)} - \boldsymbol{V}_n\right), \tag{48}$$

$$\dot{\boldsymbol{V}}_{n+\alpha_m,(i)} = \dot{\boldsymbol{V}}_n + \alpha_m\left(\dot{\boldsymbol{V}}_{n+1,(i-1)} - \dot{\boldsymbol{V}}_n\right). \tag{49}$$

2. Use the intermediate time levels of the $i$-th Newton iteration to compute the tangent matrix $\boldsymbol{K}_{,(i)}$ and the residual vector $\boldsymbol{R}_{,(i)}$. Once the tangent matrix and the residual vector are computed, the global linear system

$$\boldsymbol{K}_{,(i)}\Delta\boldsymbol{V}_{n+1,(i)} = -\boldsymbol{R}_{,(i)}, \tag{50}$$

   is solved up to a given tolerance using the GMRES method [73] with the incomplete $LU$ preconditioner [74].

3. Use $\Delta\boldsymbol{V}_{n+1,(i)}$ to update the Newton–Raphson iterates as follows

$$\boldsymbol{V}_{n+1,(i)} = \boldsymbol{V}_{n+1,(i-1)} + \Delta\boldsymbol{V}_{n+1,(i)}, \tag{51}$$

$$\dot{\boldsymbol{V}}_{n+1,(i)} = \dot{\boldsymbol{V}}_{n+1,(i-1)} + \frac{1}{\chi\Delta t}\boldsymbol{V}_{n+1,(i)}. \tag{52}$$

   This completes one nonlinear iteration.

The nonlinear iterative algorithm is repeated until the norm of each of the residual vectors $\boldsymbol{R}^\Phi$, $\boldsymbol{R}^M$, $\boldsymbol{R}^F$, $\boldsymbol{R}^G$, $\boldsymbol{R}^A$, and $\boldsymbol{R}^U$ has been reduced to a given tolerance. In our computations, we set this tolerance to $10^{-4}$.

### 3.3.2. Redefinition of the tangent matrix and the residual vector to avoid singularities

Due to the use of the diffuse domain method, we embedded the cell in a larger computational box. Outside of the cell most of the unknowns approach the value zero and the governing equations are not relevant. This increases dramatically the condition number of the tangent matrix, leading to an inefficient algorithm. The unknowns that create this problem outside the cell ($\phi \approx 0$) are $\rho_m$, $\rho_f$, and $\rho_g$. A similar situation occurs with the unknown $a$ outside of the cell membrane ($\delta_m \approx 0$). To overcome this problem we propose the following procedure. After assembling the global residual vector and tangent matrix, we proceed as follows:

i) Establish the thresholds $\phi^T = 10^{-8}$ and $\delta_m^T = 10^{-4}$ using the current nonlinear iteration of $\phi$ at the $\alpha_f$ time level; see Fig. 5.

ii) Define the spatial domains $\Omega_\phi = \{\boldsymbol{x} \mid \phi > \phi^T\}$ and $\Omega_\delta = \{\boldsymbol{x} \mid \delta_m > \delta_m^T\}$.
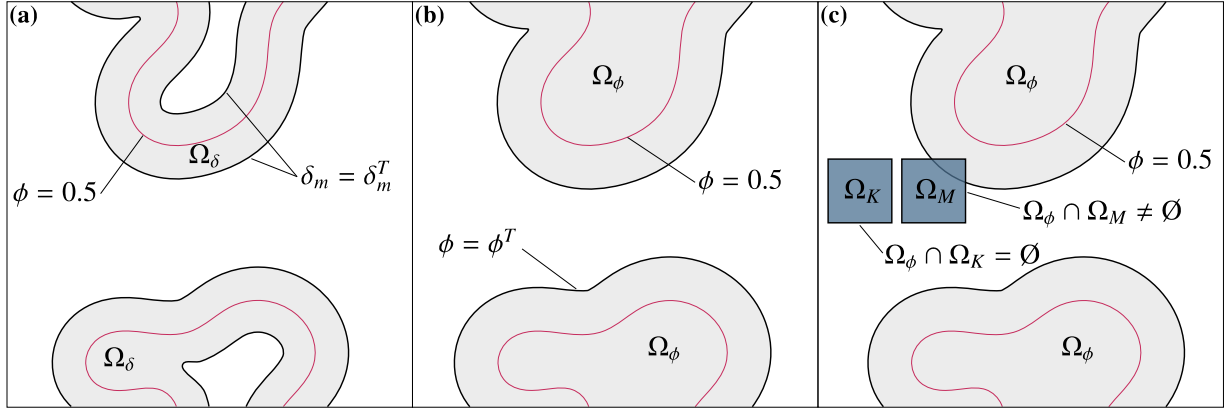
Figure 5: Different subdomains defined in our problem. (a) $\Omega_\delta$ is the region where the entries of the residual and the tangent associated to the unknown $a$ are not modified. (b) $\Omega_\phi$ is similar to $\Omega_\delta$, but for the unknowns $\rho_m$, $\rho_f$, and $\rho_g$. (c) $\Omega_M$ and $\Omega_K$ are the supports of the basis functions $N_M$ and $N_K$. $\Omega_M$ overlaps with $\Omega_\phi$, while $\Omega_K$ does not.

iii) Denote by $k_{\max} = n_b\, n_{\mathrm{dof}}$ the number of entries of the global vector of control variables $V$. Let $V_k$ be the $k$-th entry of $V$. For $k = 1, \cdots, k_{\max}$, proceed as follows:

   1. If $V_k$ is a control variable of the unknowns $\rho_m$, $\rho_f$, $\rho_g$, or $a$ associated to the basis function $N_A$, compute the support of $N_A$ and denote it by $\Omega_A$.
   2. If $\Omega_\phi \cap \Omega_A = \emptyset$ or $\Omega_\delta \cap \Omega_A = \emptyset$, then, perform the following two steps:
       2.1. Replace the row $k$ of the global tangent matrix by the row $k$ of the $k_{\max} \times k_{\max}$ identity matrix.
       2.2. Replace the $k$-th entry of the global residual vector by 0.

 iv) Solve the linear system (50) with the updated tangent matrix and residual vector.

We found that this strategy worked successfully in all our numerical examples and rendered tangent matrices with acceptable condition numbers.

**Remark 3:** Note that the entries of the tangent matrix and residual vector corresponding to velocity control variables are not modified in the procedure outlined above. This is because the adhesion force has been defined as $\boldsymbol{F}_{\mathrm{adh}} = -\varsigma \boldsymbol{u}$. This produces a contribution to the tangent matrix that is proportional to the mass matrix. Therefore, those blocks of the tangent matrix are well defined. The Stokes-type equation (34.6) essentially becomes $\varsigma \boldsymbol{u} \approx 0$ outside the cell, which leads to a vanishing velocity away from the cell. Having said this, we acknowledge that perhaps a more conceptually consistent strategy would have been to define $\boldsymbol{F}_{\mathrm{adh}} = -\varsigma \phi \boldsymbol{u}$ and use the redefinition of the tangent and residual described before also for the velocity control variables. We have opted for simplicity rather than conceptual consistency in this case.

**Remark 4:** The quantity $\Gamma_\phi c\varepsilon|\nabla\phi|$ of the phase-field equation (34.1) produces the term $-(\nabla N_A, \Gamma_\phi \varepsilon \nabla \phi) - \left(N_A, \frac{\Gamma_\phi \varepsilon}{|\nabla \phi|}\nabla \phi \cdot \nabla(|\nabla\phi|)\right)$ in the component $R_A^\Phi$ of the residual vector. At regions far from the membrane, where $|\nabla\phi| \approx 0$, the above-mentioned term of the residual as well as its contribution to the tangent are not well defined. To overcome this problem, we have set the term $\Gamma_\phi c\varepsilon|\nabla\phi|$ to zero when computing the residual and tangent in the region $\Omega_{|\nabla\phi|} = \{\, \boldsymbol{x} \mid |\nabla\phi| < |\nabla\phi|^T \,\}$ with $|\nabla\phi|^T = 10^{-5}$. In the subdomain $\Omega_{|\nabla\phi|}$, Eq. (34.1) becomes the Allen–Cahn equation [75] that keeps stable the values $\phi = 0$ and $\phi = 1$, producing the desired solution. Note that there are other ways to achieve a similar result, e.g., using for the control variables of $\phi$ the same procedure used for the control variables of $a$; see the initial part of Section 3.3.2.

**Remark 5:** To achieve accurate results in the activator equation [Eq. (34.5)] it is necessary to use a steep marker $\delta_m$ [55]. A steep marker can be obtained by taking a large value of $\varphi$ in Eq. (32), but as a consequence, the numerical approximation of the activator equation requires a very fine mesh. The requirement to use a very fine mesh can
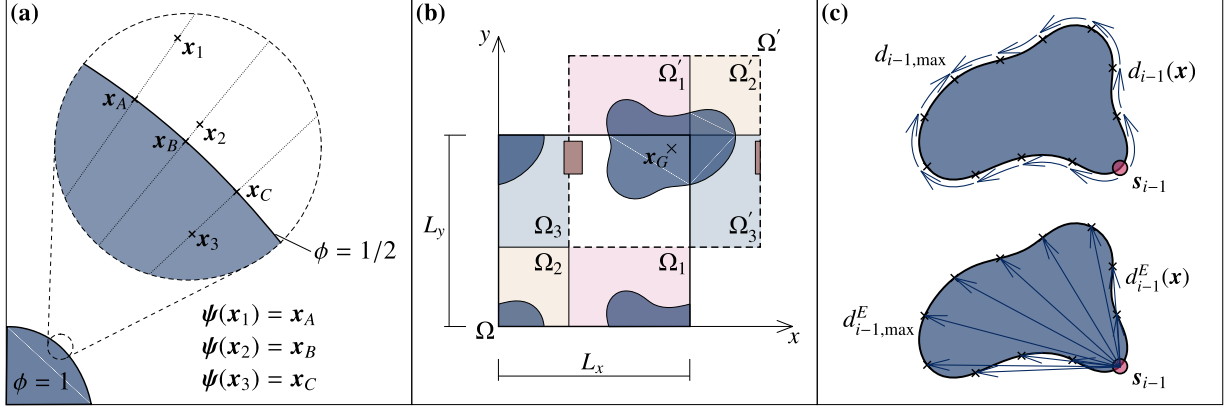
15

Figure 6: (a) Definition of the mapping $\psi$ that projects a given point to its closest point on the membrane. (b) Mapping redefining the domain. Computational domain $\Omega$ and translated domain $\Omega'$. (c) Distance to $s_{i-1}$ measured using geodesics and Euclidean distance.

be bypassed by replacing $u$ by $u^\star$ in Eq. (34.5). The field $u^\star$ can be defined as a constant extension of the field $u$ at the level set $\phi = 1/2$ in the direction orthogonal to the membrane. Mathematically, this can be expressed as $u^\star(x) = u(\psi(x))$ where $\psi(x)$ is the closest point to $x$ such that $\phi(\psi(x)) = 1/2$; see Fig. 6(a). We found that this procedure significantly speeds up the computations, introducing negligible errors. A similar procedure was also used to compute $\delta_{\text{rep}}$ in Eq. (31) where we replaced $d_o(x)$ with $d_o^\star(x) = d_o(\psi(x))$.

**Remark 6:** Our numerical experiments indicate that it may be beneficial to treat explicitly, rather than implicitly, some of the terms of the residual vector and the tangent matrix. In particular, treating explicitly $\mathcal{N}$, $\delta_f$, $\delta_{\text{rep}}$, and $u^\star$ speeds up the computations significantly without compromising the accuracy and stability of the algorithm. In all the numerical examples presented in this paper we treated $\mathcal{N}$, $\delta_f$, $\delta_{\text{rep}}$, and $u^\star$ explicitly.

**Remark 7:** The cells that we analyze in this study can move up to a distance equivalent to their diameter in one minute. Therefore, to perform simulations for a time interval of ~20 minutes, which is what we are interested on, we would need a computational box with side length 20 times larger than the cell if we want to avoid the cell touching the boundary. This is not viable from the computational point of view, so we use periodic boundary conditions. The use of periodic boundary conditions solves the problem, but we have to consider two important points: (1) The periodic box should be large enough to avoid that the cell front touches the cell back. (2) Some of the terms in the governing equations depend on distances. On a periodic box, the cell may, e.g., exit the box through the right boundary and enter again through the left side. At an intermediate step the cell may look like "broken" in the computational box. In a situation like this, we proceed as follows: Consider the 2D example presented in Fig. 6(b), in which the cell is split into four pieces. The solid square represents the computational domain $\Omega = [0, L_x] \times [0, L_y]$. Right after computing every time step, we define the domain $\Omega'$ [dashed line in Fig. 6(b)], which has the same geometry as $\Omega$, but is centered at the cell's center of mass $x_G$. Once $\Omega'$ is determined, we can define $\Omega_1$, $\Omega_2$, and $\Omega_3$ as shown in Fig. 6(b). To reconstitute the cell and all field variables in the domain $\Omega'$, we define the transformation $\Sigma(x)$ such that $x' = \Sigma(x)$ where

$$\Sigma(x) = \begin{cases} x + \{0, L_y\}^T & \text{if } x \in \Omega_1 \\ x + \{L_x, L_y\}^T & \text{if } x \in \Omega_2 \\ x + \{L_x, 0\}^T & \text{if } x \in \Omega_3 \\ x & \text{otherwise.} \end{cases} \tag{53}$$

Then, a function $f(x)$ defined in $\Omega$ can be defined in $\Omega'$ as $f\left(\Sigma^{-1}(x')\right)$. Once all the relevant fields are defined in $\Omega'$, we can directly compute distances. Note that in a problem of cellular migration with obstacles, the transformation $\Sigma$ also needs to be applied to the obstacles; see Fig. 6(b) where we represented a rigid rectangular obstacle in brown color. Although we illustrated the concept in 2D, the procedure can be easily extended to 3D problems.

16

**Remark 8:** The process described in Section 2.6 to determine the centers of the activator source ($s_i$ in our notation) requires computing the distance between two points of the cell's surface following the shortest path contained in the membrane [$d_{i-1}(\boldsymbol{x})$ in the top plot of Fig. 6(c)]. This process can be computationally expensive and, thus, an alternative is desirable. A simple strategy is to replace the distance along the membrane by the Euclidean distance [$d_{i-1}^E(\boldsymbol{x})$ in the bottom plot of Fig. 6(c)]. In our 3D computations we used the Euclidean distance rather than geodesics of the cell's membrane.

**Remark 9:** The locations of the activator sources move together with the cell's membrane. In our computations, the locations are updated using the midpoint rule and the membrane's velocity $\boldsymbol{u}^\star$. Thus, for the activator source located at $s_i$, we assume $s_i(t_{n+1}) \approx s_i(t_n) + \frac{\Delta t}{2}(\boldsymbol{u}^\star(t_n) + \boldsymbol{u}^\star(t_{n+1}))$. When we compute the residual in the Newton–Raphson loop, $\boldsymbol{u}^\star(t_{n+1})$ is replaced by the current approximation of the membrane velocity. The locations of the activator sources that enter the residual are evaluated at $\alpha_f$ time level. When the centers of the activator sources are sufficiently close to the boundary, we resort to the mapping $\Sigma$ defined in Eq. (53).

## 4. Numerical examples

In this section we present several 2D and 3D numerical examples computed using our proposed model and discretization scheme. We used different computational domains and meshes, but we took the same time step $\Delta t = 0.05$ s for all the numerical examples. The code used to perform these simulations has been developed on top of PetIGA [76, 77], which adds NURBS discretization capabilities and integration of forms to the scientific library PETCs [78].

### 4.1. Diffuse domain approach

Here, we show how the diffuse domain approach can be utilized to solve PDEs on moving domains using a fixed background mesh only. We focus on an idealized case in which a perfectly circular cell is traveling with constant velocity $\boldsymbol{u}_\phi$. Since the cell's velocity is known and fixed, we neglect the actin flow and the presence of membrane-bound components. We consider only a generic cytosolic compound $\rho_c$ that diffuses within the cell. To test the diffuse domain approach we compute a reference solution by solving the problem: Find $\rho_c : \overline{\Omega}_R \times (0, T) \to \mathbb{R}$ such that

$$\frac{\partial \rho_c}{\partial t} = D\nabla^2 \rho_c, \qquad \text{in} \quad \Omega_R \times (0, T) \tag{54.1}$$

$$\nabla \rho_c \cdot \boldsymbol{n}_{\Gamma_R} = 0, \qquad \text{on} \quad \Gamma_R \times (0, T) \tag{54.2}$$

$$\rho_c(\boldsymbol{x}, 0) = \rho_c^0(\boldsymbol{x}), \qquad \text{in} \quad \overline{\Omega}_R \tag{54.3}$$

where $\rho_c^0 : \overline{\Omega}_R \to \mathbb{R}$ is a function that represents the initial value of $\rho_c$ and $\Omega_R$ is a fixed circular domain. $\Gamma_R$ denotes the boundary of $\Omega_R$ and $\boldsymbol{n}_{\Gamma_R}$ its unit outward normal. The circle $\Omega_R$ is centered at the origin of coordinates and its radius is $10 \, \mu\text{m}$. The reference solution is computed as $\rho_c^{\text{Ref}}(\boldsymbol{x}, t) = \rho_c(\boldsymbol{x} - \boldsymbol{u}_\phi t, t)$ to account for the cell's motion. The boundary-value problem (54) is solved using a NURBS mesh that represents exactly the circular domain $\Omega_R$. We used quadratic functions with 200 elements in the circumferential direction and 100 elements in the radial direction; see Fig. 7(a).

To solve this problem using the diffuse domain method we define the box $\overline{\Omega} = [-L, L]^2$ where $L = 20 \, \mu\text{m}$ and we solve the problem: Find $\phi : \overline{\Omega} \times (0, T) \to \mathbb{R}$ and $\hat{\rho}_c : \overline{\Omega} \times (0, T) \to \mathbb{R}$ such that

$$\frac{\partial \phi}{\partial t} + \boldsymbol{u}_\phi \cdot \nabla \phi = \Gamma_\phi \left( \varepsilon \nabla^2 \phi - \frac{G'(\phi)}{\varepsilon} + c\varepsilon |\nabla \phi| \right), \qquad \text{in} \quad \Omega \times (0, T) \tag{55.1}$$

$$\frac{\partial(\phi \hat{\rho}_c)}{\partial t} + \nabla \cdot (\phi \hat{\rho}_c \boldsymbol{u}_\phi) = \nabla \cdot (D\phi \nabla \hat{\rho}_c), \qquad \text{in} \quad \Omega \times (0, T) \tag{55.2}$$

$$\phi(\boldsymbol{x}, 0) = \phi_0(\boldsymbol{x}), \qquad \text{in} \quad \overline{\Omega} \tag{55.3}$$

$$\hat{\rho}_c(\boldsymbol{x}, 0) = \rho_c^0(\boldsymbol{x}), \qquad \text{in} \quad \overline{\Omega} \tag{55.4}$$

with periodic boundary conditions in all directions. Here, $\hat{\rho}_c$ is meant to be an approximation to $\rho_c^{\text{Ref}}$ and $\phi_0 : \overline{\Omega} \to \mathbb{R}$ is a phase field that defines the initial position of the cell. More specifically, we took $\phi_0(\boldsymbol{x}) = \frac{1}{2} - \frac{1}{2}\tanh[3(d_c(\boldsymbol{x}) - 10)]$
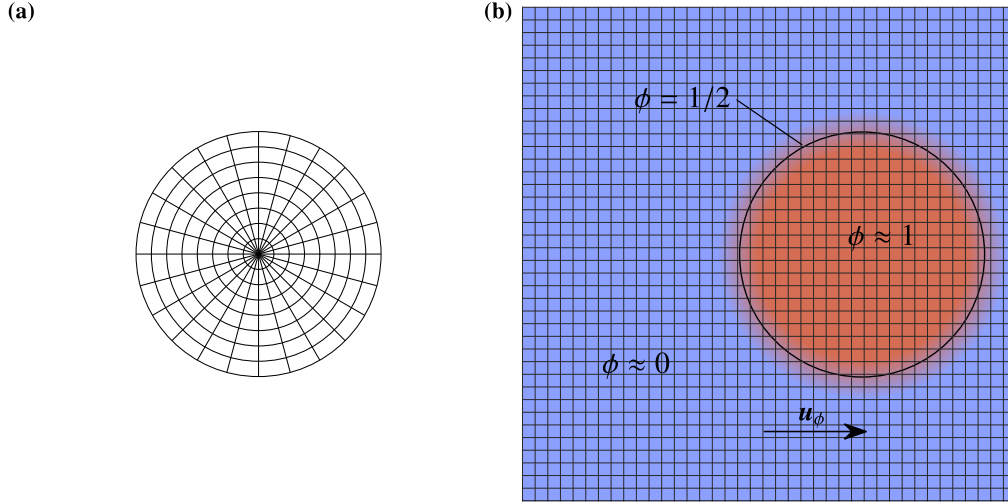
Figure 7: Diffuse domain approach. (a) NURBS mesh used to solve the boundary-value problem (54). (b) NURBS mesh used to solve problem (55) and implicit representation of the circular cell using the phase-field $\phi$. Both meshes are coarser than the meshes used in the actual computations to allow for a clearer visualization.

where $d_c(\boldsymbol{x})$ is the distance between the point $\boldsymbol{x}$ and the origin of coordinates. Note that the field $\phi_0$ takes the value ~1 in $\Omega_R$ and ~0 in the rest of the box; see Fig. 7(b). Eq. (55.1) essentially moves the cell with velocity $\boldsymbol{u}_\phi$ while maintaining a hyperbolic tangent profile in the direction orthogonal to the membrane. We meshed the computational domain $\Omega$ using $400^2$ quadratic NURBS elements.

We used the parameters $D = 10\,\mu\text{m}^2\text{s}^{-1}$ and $\boldsymbol{u}_\phi = \{0.6, 0\}^T\,\mu\text{m s}^{-1}$ for both the reference solution and the diffuse domain approach. For the diffuse domain approach we also set $\varepsilon = 1.0\,\mu\text{m}$ and $\Gamma_\phi = 0.4\,\mu\text{m s}^{-1}$, which provides a reasonable compromise between accuracy and computational time for the purpose of this paper.

We first solved the problem taking $\rho_c^0(\boldsymbol{x}) = 10H(5.0 - d_c(\boldsymbol{x}))$ where $H$ denotes the Heaviside function. Fig. 8(a) shows contour lines of $\rho_c^{\text{Ref}}$ and $\hat{\rho}_c$ in the cell's interior at times 0, 10, 20, and 30 s. The solution provided by the diffuse domain method is indistinguishable from the reference solution at the scale of the plots. More accurate results could be obtained using a finer mesh and a smaller value of $\varepsilon$.

We performed a similar computation using as initial distribution of $\rho_c$ the function $\rho_c^0(\boldsymbol{x}) = 10\exp(-0.1d_p^2(\boldsymbol{x}))$ where $d_p(\boldsymbol{x})$ denotes the distance between $\boldsymbol{x}$ and $\boldsymbol{x}_p = \{2, 0\}^T$. Using this initial condition, the solution does not exhibit circular symmetry anymore, which allows to check the accuracy of the diffuse domain method to impose the boundary condition (54.2). Fig. 8(b) shows contour lines of $\rho_c^{\text{Ref}}$ and $\hat{\rho}_c$. Again, the solutions are almost indistinguishable, but it may be observed that the error is larger close to the membrane; see, e.g., $t = 20$ s, level set 0.25.

In all, this example shows that the diffuse domain method can be safely used for cellular migration problems, introducing negligible errors with respect to the uncertainties in the biological model and the values of the parameters.

### 4.2. Mesenchymal cellular motion

In preparation for our simulations of amoeboid cellular motion, we first exercise our computational method on a simpler problem, namely, mesenchymal migration [2, 13]. A phase-field model of mesenchymal motion can be derived from our theory of amoeboid motion simply neglecting the activator equation and setting $I(a) = 0$ in Eq. (7). This model is considerably simpler than that of amoeboid motion because we do not need to resolve the dynamics of the activator on the membrane. However, mesenchymal cell migration is a very interesting problem in its own right and one that has triggered significant interest in the experimental and theoretical communities. Mesenchymal motion is usually studied by way of experiments with *keratocytes* [36, 79, 80]. These cells move spontaneously (without any external stimulus) over flat substrates by extending a stationary lamellipodium at the leading edge. As we show later, keratocytes exhibit a variety of different motions that the model replicates. Unless otherwise stated, for the numerical
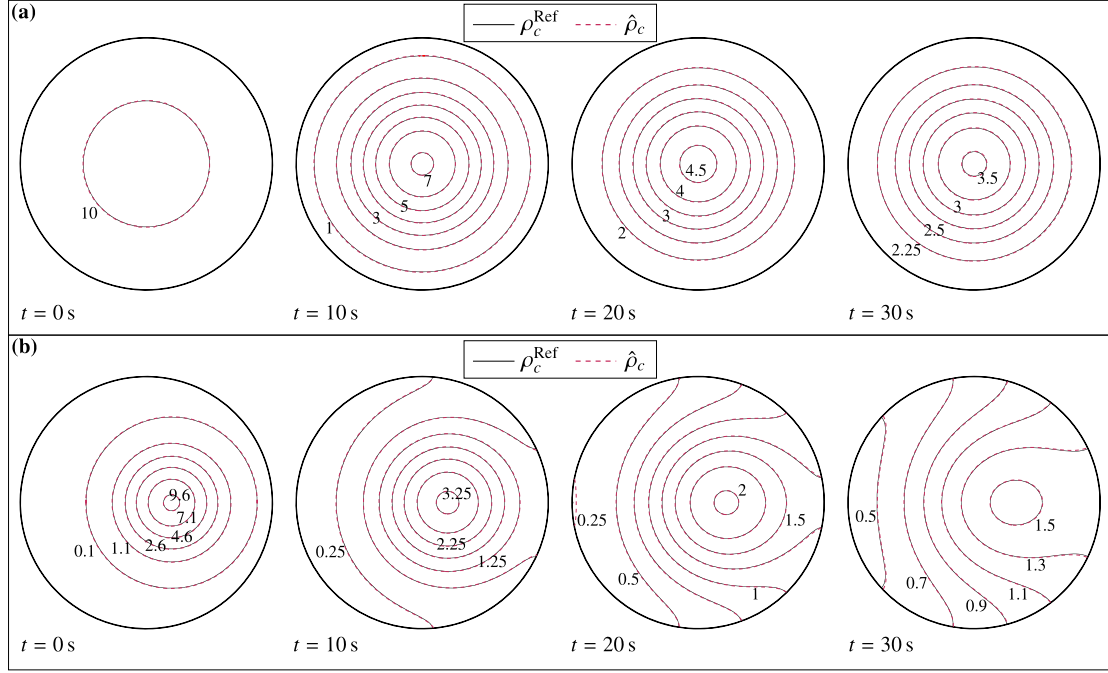
Figure 8: Diffusion of a chemical substance in a perfectly circular cell moving with constant velocity. Comparison of the classical method that uses a mesh conforming to the geometry of the cell ($\rho_c^{\text{Ref}}$, black line) and the diffuse domain method which uses a fixed background mesh ($\hat{\rho}_c$, pink line). (a) Solutions corresponding to the initial condition $\rho_c^0(\boldsymbol{x}) = 10H(5.0 - d_c(\boldsymbol{x}))$. (b) Solutions corresponding to the initial condition $\rho_c^0(\boldsymbol{x}) = 10\exp(-0.1 d_p^2(\boldsymbol{x}))$.

examples of mesenchymal cellular motion we used the computational domain $\overline{\Omega} = [-L, L]^2$ with $L = 20\,\mu\text{m}$ and a mesh composed of 200 $C^1$-continuous quadratic elements in each direction.

### 4.2.1. Stationary states of free movement

Consistently with what is observed in experiments of keratocytes, our model of mesenchymal motion predicts stationary states of free motion[5]. These stationary states correspond to a cell that migrates with constant velocity and fixed shape. To understand how the equilibrium cell shapes and velocities depend on the parameters, we conducted several simulations. The values of all the model parameters except $\overline{\eta}_m$ and $\overline{\eta}_f$ (which are used for a parametric study) are listed in Table 1. In addition, we initially assumed that $K_c = 0$. We will show later that this hypothesis is acceptable.

The initial conditions are the same in all simulations. They represent a circular cell of radius $r_c = 9\,\mu\text{m}$ with vanishing velocity and uniform distribution of myosin and G-actin densities. The distribution of F-actin is non-uniform to produce the cell's polarization and trigger the motion. Specifically, we take

$$\phi(\boldsymbol{x}, 0) = 0.5 - 0.5\tanh[1.5(d_c(\boldsymbol{x}) - r_c)], \tag{56.1}$$

$$\rho_m(\boldsymbol{x}, 0) = \phi(\boldsymbol{x}, 0), \tag{56.2}$$

$$\rho_f(\boldsymbol{x}, 0) = \begin{cases} 1.5\,\phi(\boldsymbol{x}, 0) & \text{if } y \geq 0, \\ 0.5\,\phi(\boldsymbol{x}, 0) & \text{if } y < 0, \end{cases} \tag{56.3}$$

$$\rho_g(\boldsymbol{x}, 0) = 1.1\,\phi(\boldsymbol{x}, 0), \tag{56.4}$$

$$\boldsymbol{u}(\boldsymbol{x}, 0) = 0, \tag{56.5}$$

---

[5]By free motion we refer to migration on a planar substrate without obstacles.

19

Table 1: Keratocyte motion parameters

| Symbol | Description | Value |
|--------|-------------|-------|
| $\Gamma_\phi$ | Parameter enforcing a hyperbolic tangent profile | $0.52\,\mu\text{m s}^{-1}$ |
| $\varepsilon$ | Phase-field interfacial length scale | $2\,\mu\text{m}$ |
| $D_{\max}$ | Myosin diffusion scale | $4.16\,\mu\text{m}^2\text{s}^{-1}$ |
| $K$ | Decay rate of mysosin diffusion | $1.55\,\mu\text{m}^2$ |
| $\varepsilon_f$ | Diffusive length scale of F-actin | $0.707\,\mu\text{m}$ |
| $\varepsilon_g$ | Diffusive length scale of G-actin | $3.16\,\mu\text{m}$ |
| $\alpha$ | Penalty parameter for actin conservation | $0.06\,\mu\text{m}^{-2}$ |
| $\Gamma_f$ | F-actin mobility | $0.52\,\text{s}^{-1}$ |
| $\Gamma_g$ | G-actin mobility | $0.52\,\text{s}^{-1}$ |
| $\mu$ | Dynamic viscosity coefficient | $1500\,\text{pN s}\,\mu\text{m}^{-1}$ |
| $\lambda$ | Bulk viscosity coefficient | $-500\,\text{pN s}\,\mu\text{m}^{-1}$ |
| $A$ | Range of contractile forces | $1.0$ |
| $B$ | Range of protrusive forces | $0.07659$ |
| $\varsigma$ | Substrate friction coefficient | $0.7\,\text{pN s}\,\mu\text{m}^{-3}$ |
| $\gamma$ | Surface tension coefficient | $50\,\text{pN}$ |

where $d_c(\boldsymbol{x})$ represents the distance between $\boldsymbol{x}$ and the coordinates origin. All the simulations reach a stationary state at time $t \approx 120\,\text{s}$. Figs. 9 and 10 show, respectively, the stationary F-actin ($\rho_f$) and myosin ($\rho_m$) distributions for different values of $\overline{\eta}_m$ and $\overline{\eta}_f$. The plots show the cell's polarization: while the lamellipodium (associated to areas of large F-actin concentration) is pushing the front of the cell (Fig. 9), myosin is located at the back of the cell (Fig. 10) producing its contraction. The different equilibrium shapes adopted by the cell depend on the balance between protrusive and contractile forces. The three simulations corresponding to $\overline{\eta}_f = 2000\,\text{pN}\,\mu\text{m}^3$ (see Figs. 9 or 10) clearly show the influence of $\overline{\eta}_m$. For higher values of $\overline{\eta}_m$, which produce greater contractile forces exerted by myosin, the cell even loses its convex shape (bottom row, middle column). Increasing the value of $\overline{\eta}_f$ the lack of convexity can be alleviated as shown in the bottom-right panel. The bottom left image corresponds to an extreme case in which the contractile forces are so strong compared to the protrusive ones that the cell loses its polarization and the lamellipodium extends all over the cytoplasm. However, myosin is still concentrated at the back of the cell, which produces a slow steady motion.

Fig. 11 shows the stationary velocity field for all values of $\overline{\eta}_m$ and $\overline{\eta}_f$. The color scale represents the velocity magnitude. We also added arrows at random locations. The plots show that the lamellipodium undergoes retrograde flow as observed in experiments [36]; see, in particular, the zoomed in region in the central panel. The zoomed in area clearly shows that the membrane velocity points upwards, but the velocity at nearby points of the cytosol has opposite sign. Fig. 12 displays the area, aspect ratio (width/length), and the global velocity of the cell for the stationary states. We can see that if the cell is fully polarized, its area remains fairly constant [Fig. 12(a)]. The aspect ratio increases as contractile forces become larger with respect to protrusive forces, except when the cell is not fully polarized. As expected, the unpolarized cell breaks the trend again; see Fig. 12(b). The cell's velocity increases with increasing values of protrusive forces and with decreasing values of contractile forces. This is true even in the case of the unpolarized cell.

To finalize this example, we compute again some of the stationary states using different values for the bending rigidity $K_c$. We will show that the bending rigidity of the membrane does not play a significant role in the solution as anticipated. We maintained the time step and the number of elements, but now we use cubic splines with $C^2$ global continuity to be able to generate discrete spaces in $\mathcal{H}^3$ and compute the integrals in Eq. (37). Fig. 13 shows the results along with the control parameters for the analysis (all examples correspond to $\overline{\eta}_f = 2000\,\text{pN}\,\mu\text{m}^3$). The figure also shows the cell's equilibrium shape by displaying the level set $\phi = 1/2$. We observe that even the value $K_c = 80\,\text{pN}\,\mu\text{m}^2$, which is much greater than measured values [81, 82], produces negligible variations of the equilibrium shape. Fig. 14 shows that the cell's area, aspect ratio, and global velocity depend on the bending rigidity very mildly. We conclude, in agreement with other computational works [31], that bending forces can be neglected in the computations. Therefore, all the subsequent computations in this paper assume $K_c = 0$. From the computational point of view, this has the
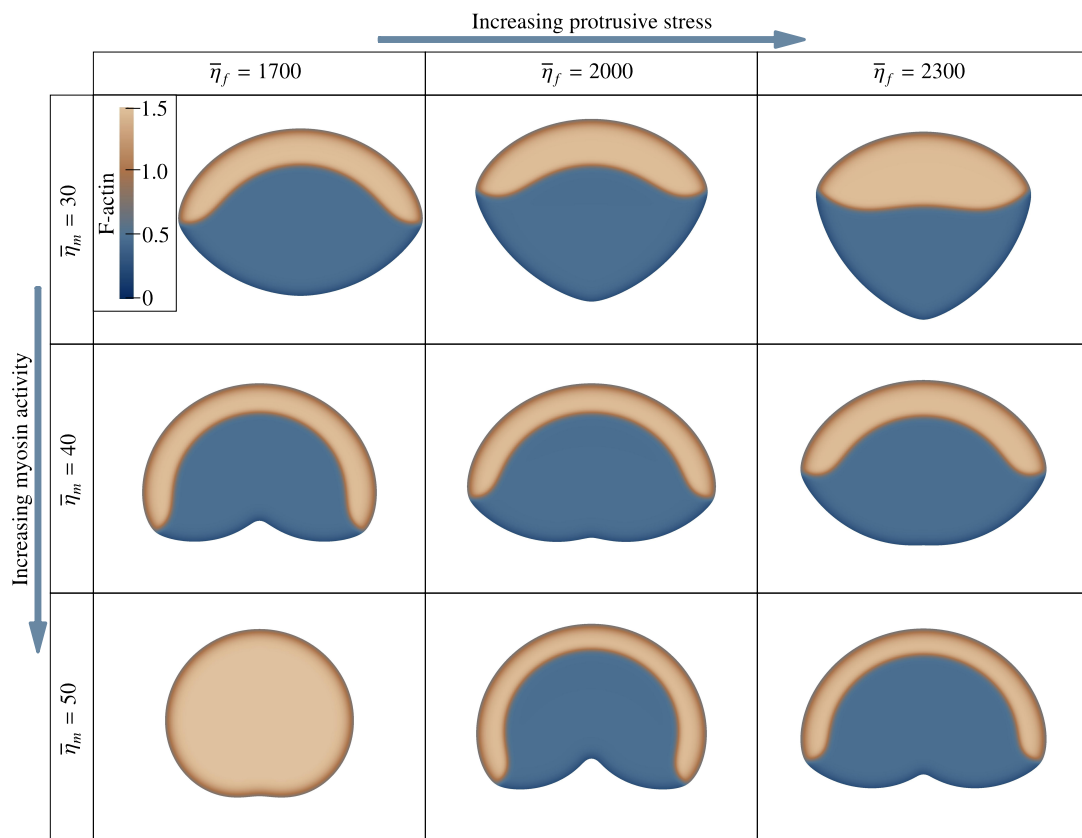
Figure 9: Mesenchymal cellular migration. Stationary states of keratocyte free motion. The equilibrium cell shape depends on the balance between contractile and protrusive forces. The color scale represents the F-actin density.
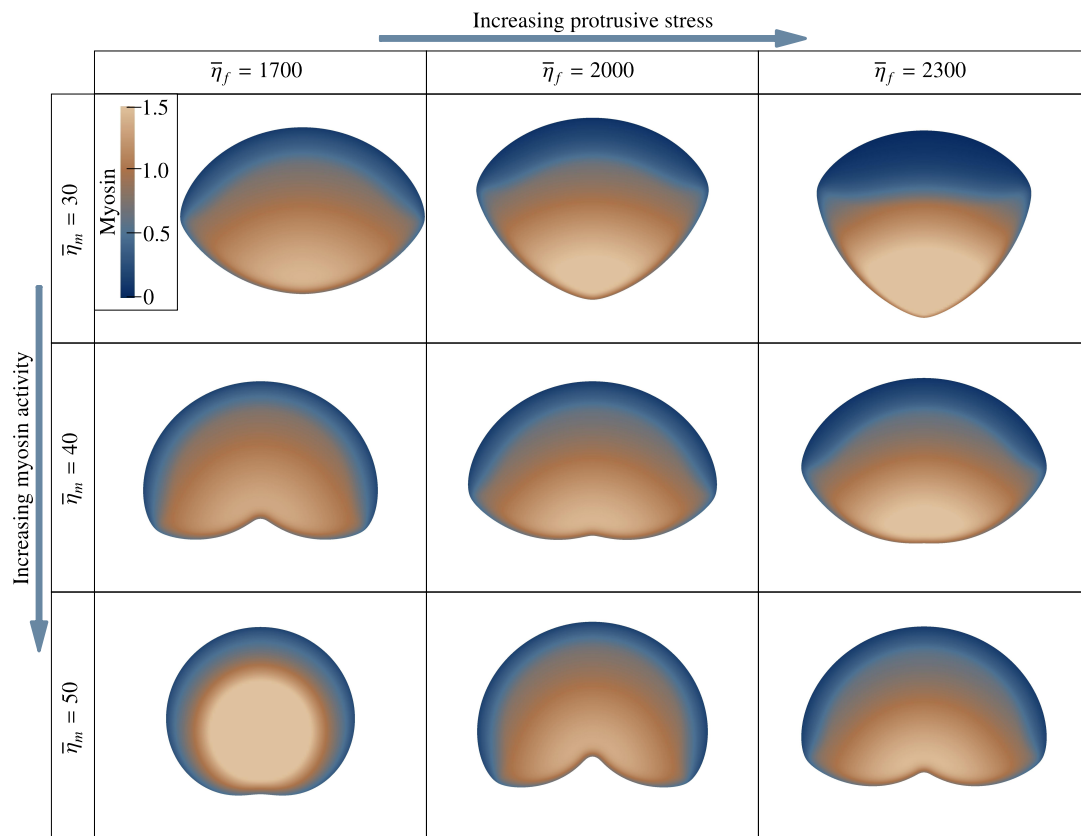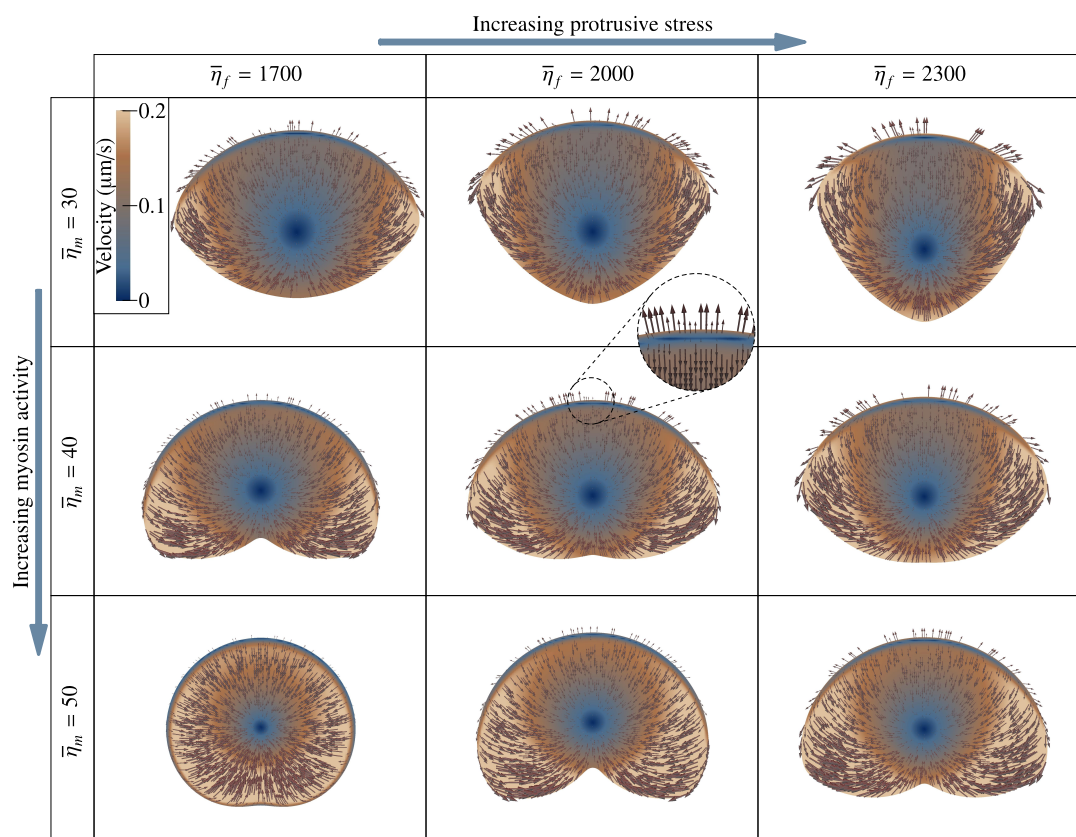
Figure 10: Mesenchymal cellular migration. Stationary states of keratocyte free motion. The equilibrium cell shape depends on the balance between contractile and protrusive forces. The color scale represents the myosin density.

Figure 11: Mesenchymal cellular migration. Stationary states of keratocyte free motion. The equilibrium cell shape depends on the balance between contractile and protrusive forces. The color scale represents the velocity magnitude. In some random points, we also show the velocity field with arrows.
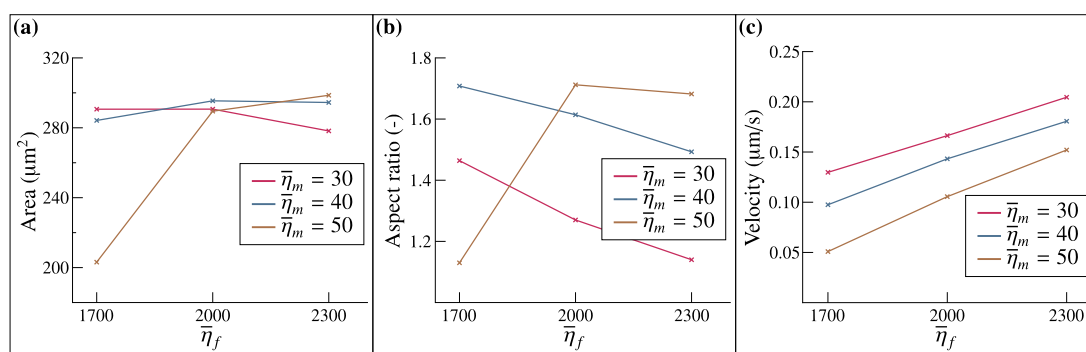


Figure 12: Mesenchymal cellular migration. Stationary states of keratocyte free motion. (a) Area of the cell. (b) Aspect ratio. (c) Global cell velocity.
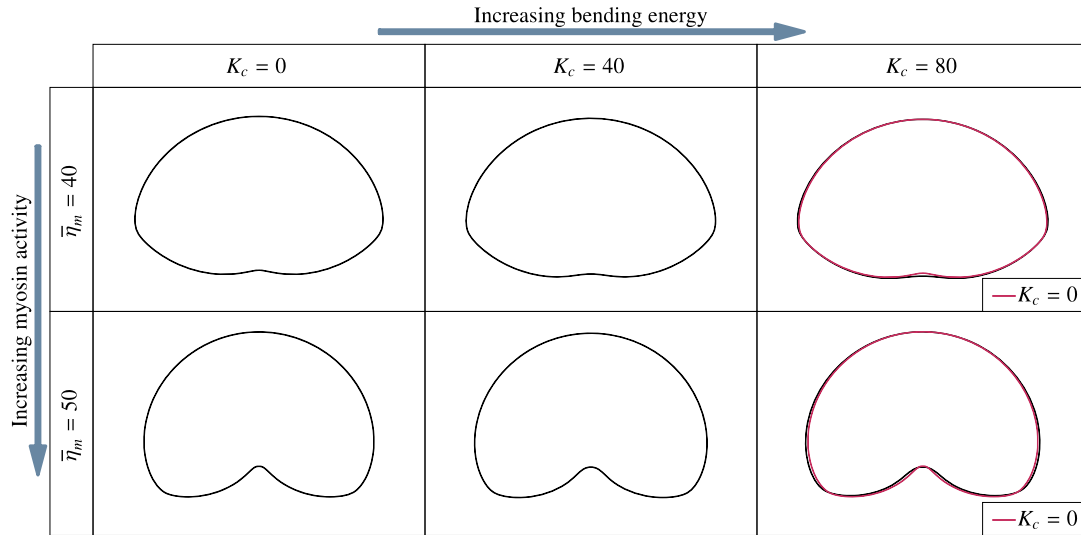
Figure 13: Mesenchymal cellular migration. Influence of the membrane's bending resistance on the stationary cell shape for different values of $\bar{\eta}_m$. The cell is represented by the level set $\phi = 1/2$. The rightmost column shows the solutions for $K_c = 80\,\mathrm{pN\,\mu m^2}$ (black line) and $K_c = 0$ (red line).
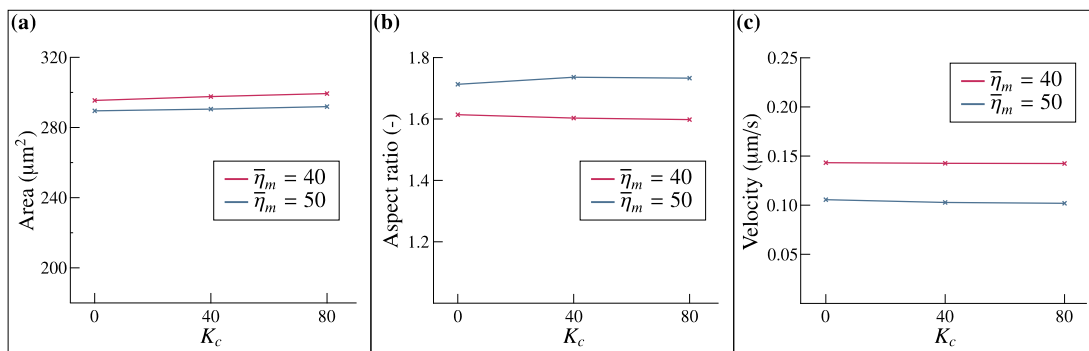


Figure 14: Mesenchymal cellular migration. Influence of the membrane's bending rigidity. (a) Area of the cell. (b) Aspect ratio. (c) Cell's global velocity.
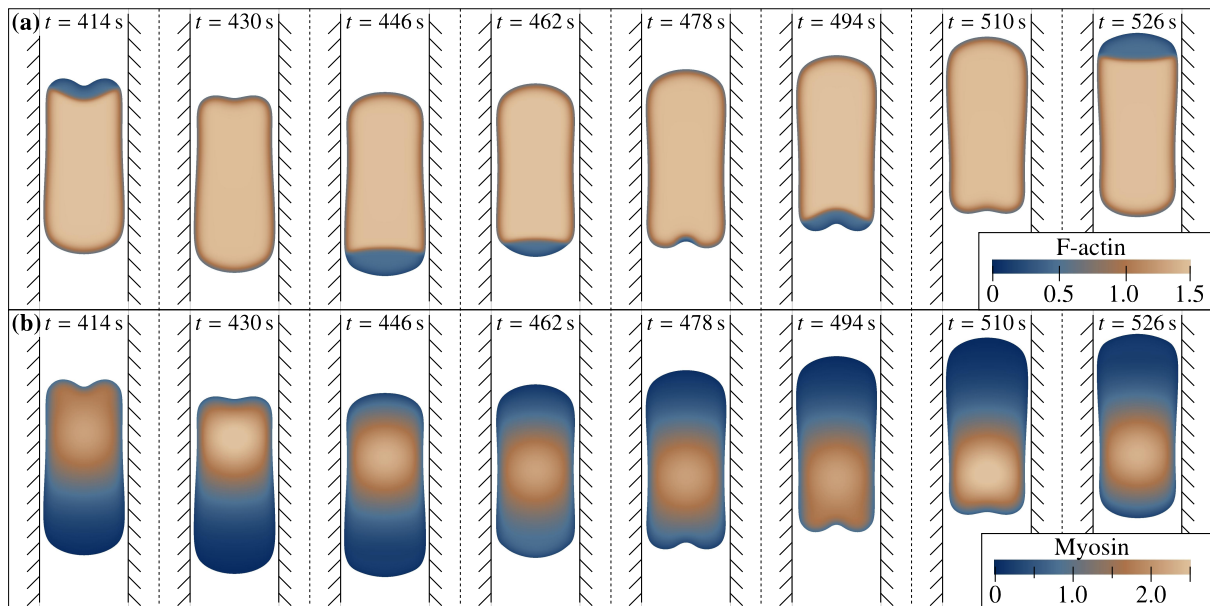
24

Figure 15: Mesenchymal cellular migration. Oscillatory motion of keratocytes in a microchannel. (a) F-actin distribution. (b) Myosin distribution.

advantage that $C^1$-continuous quadratic functions can be used in the computations. This reduces the computational time in our implementation.

### 4.2.2. Oscillatory motion of keratocytes in a microchannel

This section shows that our model can reproduce oscillatory motion of keratocytes confined in a microchannel geometry [52]. We place a microchannel of width $10\,\mu m$ oriented in the vertical direction and symmetrically located in the domain. The microchannel walls are modeled as two linear obstacles that exert forces on the cell through the term $\boldsymbol{F}_{\text{rep}}$ in Eq. (10). We place a polarized, elongated cell in the interior of the microchannel and let the simulation evolve. The cell displays an oscillatory motion which alternates migrations downwards and upwards in the channel. The model parameters are defined in Table 1 with $\eta_{\text{rep}} = 4550\,\text{pN}\,\mu m$, $\bar{\eta}_f = 2000\,\text{pN}\,\mu m^3$, and $\bar{\eta}_m = 30\,\text{pN}\,\mu m$. The initial conditions are:

$$\phi(\boldsymbol{x}, 0) = \left\{0.5 - 0.5\tanh[1.5(|x| - w/2)]\right\}\left\{0.5 - 0.5\tanh[1.5(|y| - l/2)]\right\}, \tag{57.1}$$

$$\rho_m(\boldsymbol{x}, 0) = \begin{cases} 0 & \text{if } y \geq 0, \\ 2.1\,\phi(\boldsymbol{x}, 0) & \text{if } y < 0, \end{cases} \tag{57.2}$$

$$\rho_f(\boldsymbol{x}, 0) = \begin{cases} 1.5\,\phi(\boldsymbol{x}, 0) & \text{if } y \geq 0, \\ 0.5\,\phi(\boldsymbol{x}, 0) & \text{if } y < 0, \end{cases} \tag{57.3}$$

$$\rho_g(\boldsymbol{x}, 0) = 1.1\,\phi(\boldsymbol{x}, 0), \tag{57.4}$$

$$\boldsymbol{u}(\boldsymbol{x}, 0) = 0, \tag{57.5}$$

where $w = 10\,\mu m$ and $l = 20\,\mu m$ are, respectively, the width ($x$-direction size) and the length ($y$-direction size) of the cell. Note that the initial distributions of F-actin and myosin correspond to those of a polarized cell. Figs. 15(a) and (b) show, respectively, the distributions of F-actin and myosin at several times. For a clearer visualization, we only show the relevant part of the computational domain. The snapshots corresponding to $t = 414\,\text{s}$ and $t = 494\,\text{s}$ represent a similar cell shape as well as F-actin and myosin distributions, but with the cell moving in opposite directions. Fig. 16 shows the time evolution of the cell's area, its global (vertical) velocity, and the $y$-coordinate of its center of mass. We observe that the cell's area [Fig. 16(a)] displays variations of up to ~15% as observed in experiments [79]. Fig. 16(b) shows that the vertical velocity changes sign periodically, producing the oscillatory motion. Between each two sign
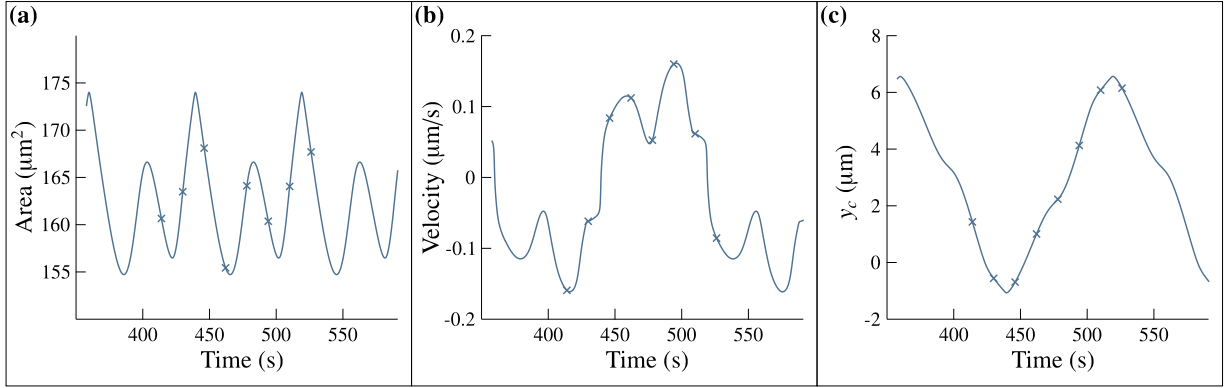
25

Figure 16: Mesenchymal cellular migration. Oscillatory motion of keratocytes in a microchannel. (a) Area of the cell. (b) Global velocity. (c) $y$-coordinate of the cell's mass center. The cross marks in the plots correspond to the snapshots in Fig. 15.

changes the velocity presents a non-trivial time evolution; see, e.g., the time interval $t \in [440, 515]$. The reason for this is that when F-actin depolarizes for the first time in the time interval ($t \approx 478$ s) myosin has not moved to the back of the cell yet and the cell gets polarized in the same direction again ($t \approx 494$ s). When F-actin depolarizes for the second time ($t \approx 510$ s) myosin is at the back and the cell is able to reverse motion. The time evolution of the vertical position of the cell's center of mass [$y_c$ in Fig. 16(c)] is simpler and shows a plain oscillatory motion with period $\sim$160 s. By modifying the parameters $\overline{\eta}_f$ or $\overline{\eta}_m$ the model can produce oscillatory motions with different periods as well as stick-slip motion [49] (data not shown).

### 4.2.3. Bipedal motion of keratocytes in a microchannel

Using exactly the same setup as in the previous example and changing the initial conditions only, the model predicts bipedal motion [83]. The initial cell's position defined by $\phi(\boldsymbol{x}, 0)$ is the same as before [see Eq. (57.1)]. The initial velocity is set to zero as in Eq. (57.5) and the G-actin density is given by Eq. (57.4). The distributions of myosin and F-actin are given by

$$\rho_m(\boldsymbol{x}, 0) \;=\; \phi(\boldsymbol{x}, 0), \tag{58.1}$$

$$\rho_f(\boldsymbol{x}, 0) \;=\; \begin{cases} 1.5\,\phi(\boldsymbol{x}, 0) & \text{if } y \geq -2x, \\ 0.5\,\phi(\boldsymbol{x}, 0) & \text{if } y < -2x. \end{cases} \tag{58.2}$$

The reason why these initial conditions enable bipedal motion is that the F-actin distribution is non-symmetric in the vertical and horizontal directions. Figs. 17(a) and (b) show several snapshots of the F-actin and myosin distributions while the cell is moving upwards. It may be observed that the back part of the cell leaves behind a tail that oscillates from left to right giving rise to the bipedal motion. The plots show that the cell remains polarized throughout the entire time interval although the lamellipodium extends over a large area of the cytosol. Figs. 18(a) and (b) show, respectively, the time evolution of the cell's area and the $x$- and $y$-position of its center of mass. Fig. 18(b) shows that the bipedal motion is characterized by a quasi-constant vertical velocity and an oscillatory retraction of one side of the cell body out of phase with the other side [83] – the latter is reflected in the time evolution of the $x$-coordinate of the cell's center of mass. Fig. 18(c) shows the trajectory of the cell's center of mass.

### 4.3. Amoeboid cellular motility

This section shows numerical examples of amoeboid motion. We will focus on a particular type of cell, namely, *Dictyostelium discoideum*. This cell type has been widely studied by the experimental community and is starting to trigger interest in computational physics and computational mechanics. The examples presented in this section include an additional layer of complexity with respect to those presented so far in the paper. The reason is that now we consider the membrane-bound species, whose dynamics is controlled by Eq. (33). Therefore, we solve the governing equations as described in Section 3 with the only assumption that bending forces are negligible – this
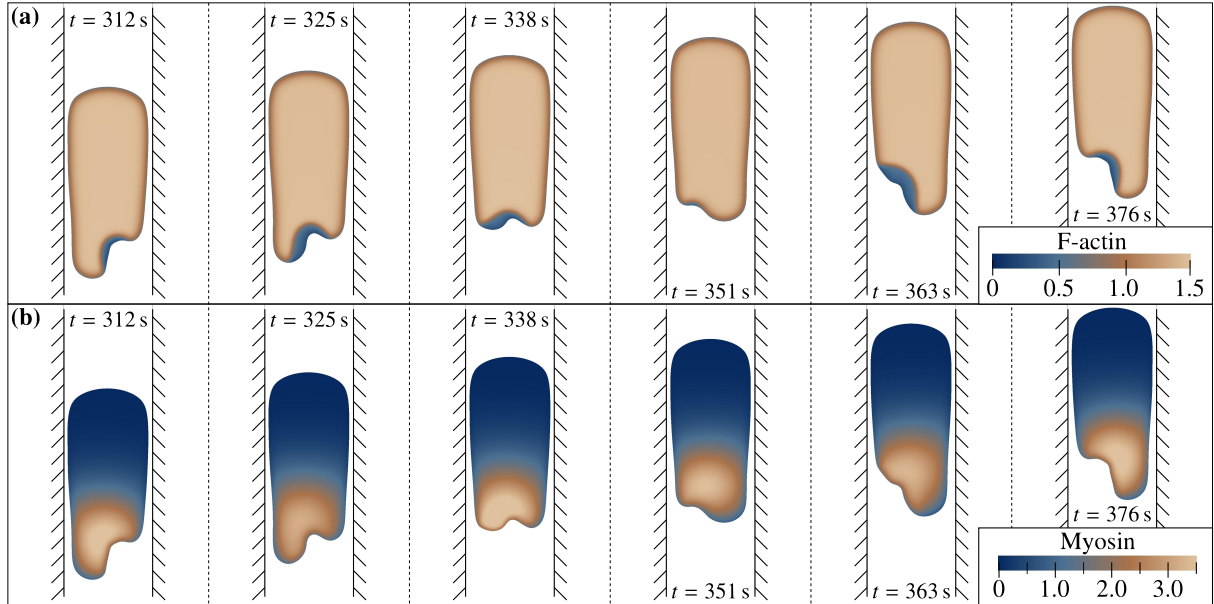
26

Figure 17: Mesenchymal cellular migration. Bipedal motion of keratocytes in a microchannel. (a) F-actin distribution. (b) Myosin distribution.
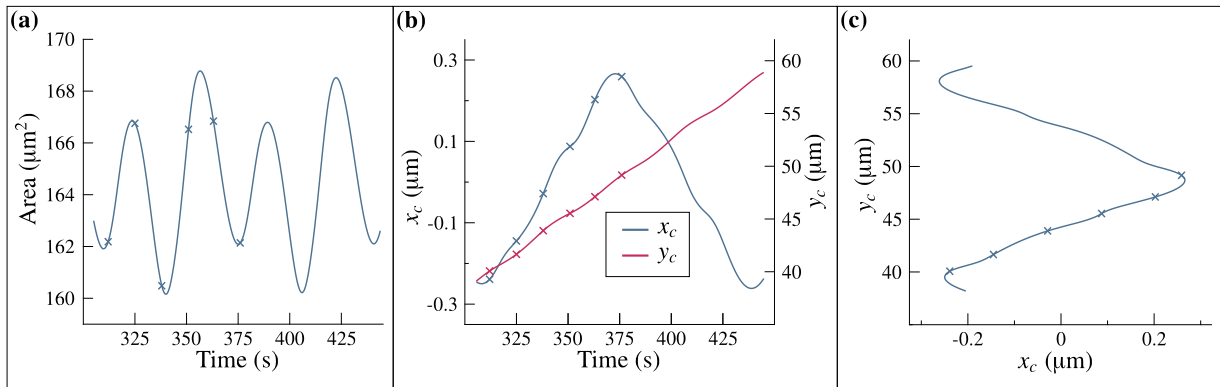


Figure 18: Mesenchymal cellular migration. Bipedal motion of keratocytes in a microchannel. (a) Time evolution of the cell's area. (b) Time evolution of the position of the cell's center of mass ($x$ and $y$-coordinates). (c) Trajectory of the cell. The cross marks in the plots correspond to the snapshots in Fig. 17.

Table 2: Dictyostelium motion parameters

| Symbol | Description | Value |
|--------|-------------|-------|
| $\Gamma_\phi$ | Parameter enforcing a hyperbolic tangent profile | $0.52\,\mu\text{m}\,\text{s}^{-1}$ |
| $\varepsilon$ | Phase-field interfacial length scale | $2\,\mu\text{m}$ |
| $D_{\max}$ | Myosin diffusion scale | $4.16\,\mu\text{m}^2\text{s}^{-1}$ |
| $K$ | Decay rate of mysosin diffusion | $1.55\,\mu\text{m}^2$ |
| $\varepsilon_f$ | Diffusive length scale of F-actin | $0.707\,\mu\text{m}$ |
| $\varepsilon_g$ | Diffusive length scale of G-actin | $3.16\,\mu\text{m}$ |
| $\alpha$ | Penalty parameter for actin conservation | $0.06\,\mu\text{m}^{-2}$ |
| $\Gamma_f$ | F-actin mobility | $0.52\,\text{s}^{-1}$ |
| $\Gamma_g$ | G-actin mobility | $0.52\,\text{s}^{-1}$ |
| $D_a$ | Diffusion coefficient of activator | $0.195\,\mu\text{m}^2\text{s}^{-1}$ |
| $r_a$ | Decay rate of activator | $0.325\,\text{s}^{-1}$ |
| $b_a$ | Production rate of activator | $7.8\,\text{s}^{-1}$ |
| $\varphi$ | Scaling of membrane marker width | $25$ |
| $a_{\max}$ | Saturation of activator | $1.5\,\mu\text{m}^{-2}$ |
| $r_p$ | Radius of activator source | $1\,\mu\text{m}$ |
| $\Delta T_i$ | Growth time of pseudopods | See Fig. 4(a) |
| $\Delta\tau_i$ | Time interval between pseudopods | See Fig. 4(b) |
| $\mu$ | Dynamic viscosity coefficient | $1500\,\text{pN}\,\text{s}\,\mu\text{m}^{-1}$ |
| $\lambda$ | Bulk viscosity coefficient | $-500\,\text{pN}\,\text{s}\,\mu\text{m}^{-1}$ |
| $\bar{\eta}_m$ | Strength of contractile forces | $22.1\,\text{pN}\,\mu\text{m}$ |
| $A$ | Range of contractile forces | $0.4117$ |
| $\bar{\eta}_f$ | Strength of protrusive forces | $1.22\cdot10^4\,\text{pN}\,\mu\text{m}^3$ |
| $B$ | Range of protrusive forces | $0.07659$ |
| $\varsigma$ | Substrate friction coefficient | $0.7\,\text{pN}\,\text{s}\,\mu\text{m}^{-3}$ |
| $\gamma$ | Surface tension coefficient | $78\,\text{pN}$ |
| $\eta_{\text{rep}}$ | Strength of repulsive forces | $4550\,\text{pN}\,\mu\text{m}$ |

assumption has been verified numerically in Section 4.2.1 for mesenchymal motion. We suppose it also holds true for amoeboid motion.

We present two simulations in 2D and one in 3D. The first 2D simulation shows free amoeboid motion while the second one takes place in an environment with rigid obstacles. For the 2D simulations, we always used the computational domain $\overline{\Omega} = [-L, L]$ with $L = 20\,\mu\text{m}$. We meshed this domain using 200 $C^1$-continuous quadratic elements in each direction. The 3D simulation studies amoeboid migration in a fibrous medium.

### 4.3.1. Dictyostelium free movement

We analyze how *Dictyostelium* moves spontaneously without any chemoattractants as observed in experiments [61]. To simplify the analysis, we start studying motion on a planar substrate without obstacles. We assume periodic boundary conditions in all directions. The parameter values used in the 2D simulations of amoeboid motion are shown in Table 2. In this example, the initial conditions can be written as

$$\phi(\boldsymbol{x}, 0) = 0.5 - 0.5\tanh[1.5(d_c(\boldsymbol{x}) - r_c)], \tag{59.1}$$

$$\rho_m(\boldsymbol{x}, 0) = \phi(\boldsymbol{x}, 0), \tag{59.2}$$

$$\rho_f(\boldsymbol{x}, 0) = 0.5\,\phi(\boldsymbol{x}, 0), \tag{59.3}$$

$$\rho_g(\boldsymbol{x}, 0) = 1.1\,\phi(\boldsymbol{x}, 0), \tag{59.4}$$

$$a(\boldsymbol{x}, 0) = 0, \tag{59.5}$$

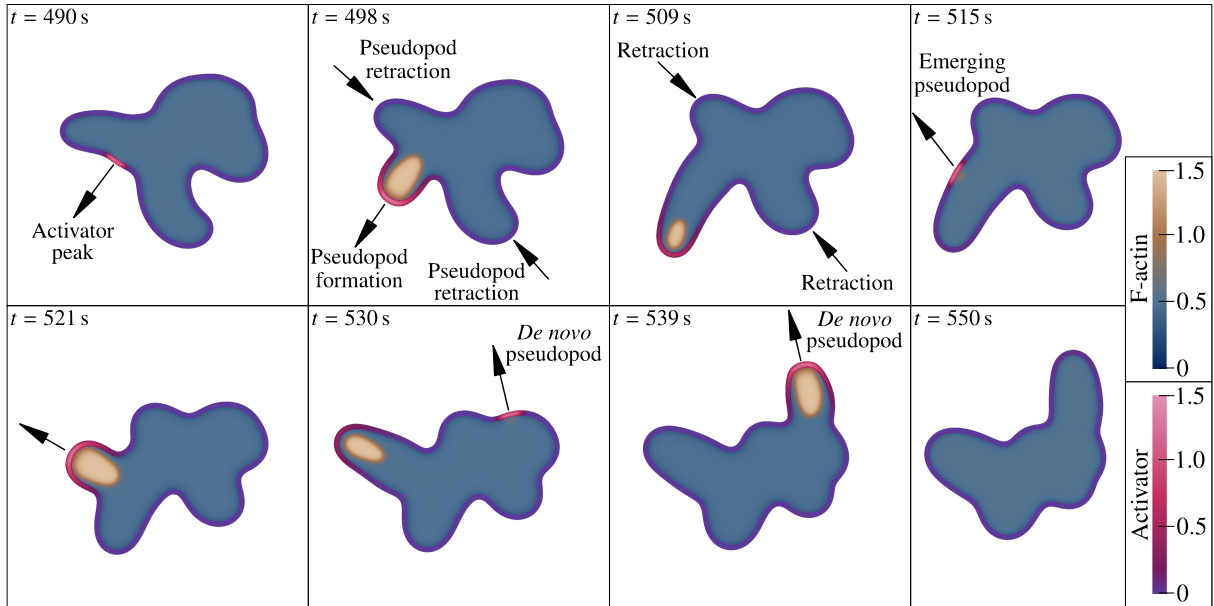$$\boldsymbol{u}(\boldsymbol{x}, 0) = 0, \tag{59.6}$$

Figure 19: Amoeboid cellular motion. *Dictyostelium* free movement. Time evolution of the F-actin and activator distributions. The arrows indicate the extension or retraction of pseudopods.

where $d_c(\boldsymbol{x})$ denotes the distance between $\boldsymbol{x}$ and the origin of coordinates and $r_c = 8.2\,\mu\mathrm{m}$ is the cell's radius. The initial conditions represent an unpolarized circular cell. We anticipate that amoeboid motion is very different from the mesenchymal motion that we have simulated up to now. While keratocytes present a stationary lamellipodium and a fairly constant cellular shape, *Dictyostelium* undergoes a highly dynamic motion with a very well orchestrated process of growth and retraction of pseudopods. Fig. 19 shows several snapshots of the moving cell. In the cell's interior the color scale represents F-actin density. We have also plotted a strip at the cell's membrane. The color of the strip represents the activator concentration. As expected, a peak in the activator concentration ($t = 490\,\mathrm{s}$) produces a region with high F-actin density in a nearby area of the cell's interior ($t = 498\,\mathrm{s}$). High F-actin concentration is associated to protrusive structures that push the membrane outwards giving rise to a pseudopod. Simultaneously, the previous pseudopods retract ($t = 498\,\mathrm{s}$ and $t = 509\,\mathrm{s}$). The process is periodically repeated with most new pseudopods emerging at the front of the cell as described by the probability distributions displayed in Figs. 4(d)–(f). This is a particular feature of amoeboid motility that produces *persistent* motion. However, occasionally, a new protrusive structure grows far from the cell's front giving rise to a so-called *de novo* pseudopod [62], which produces an abrupt change of direction in the cell ($t = 530\,\mathrm{s}$ and $t = 539\,\mathrm{s}$). Fig. 20 shows the myosin distribution and the membrane's velocity at the same time steps. The plots show how myosin is mostly concentrated at the rear of the cell [3], producing the contraction of the tail as well as the retraction of the pseudopods that are no longer active.

### 4.3.2. Dictyostelium migration on a planar surface with obstacles

*Dictyostelium* cells are known to migrate effectively on a planar substrate with obstacles. This example shows that the model can successfully reproduce this feature of amoeboid motion. The model parameters are again listed in Table 2. The initial conditions and the boundary conditions are the same as in Section 4.3.1. The top left panel of Fig. 21 shows the computational domain represented by a square plotted with dashed lines. For visualization purposes, we have periodically extended the computational domain in both directions, so that the top left panel of Fig. 21 is approximately four times larger than the actual computational domain. The obstacles have rectangular shape, random locations, and have been plotted with brown color. The blue, red, and green squares in the top left panel represent the areas that will be plotted in the rest of the top row, the middle row, and the bottom row, respectively. The color scales in Fig. 21 represent the F-actin and activator concentrations. The first row of the figure shows how the central obstacle exerts forces on the cell; see the term $\boldsymbol{F}_{\mathrm{rep}}$ in Eq. (10). These forces bend the cell's membrane, avoiding
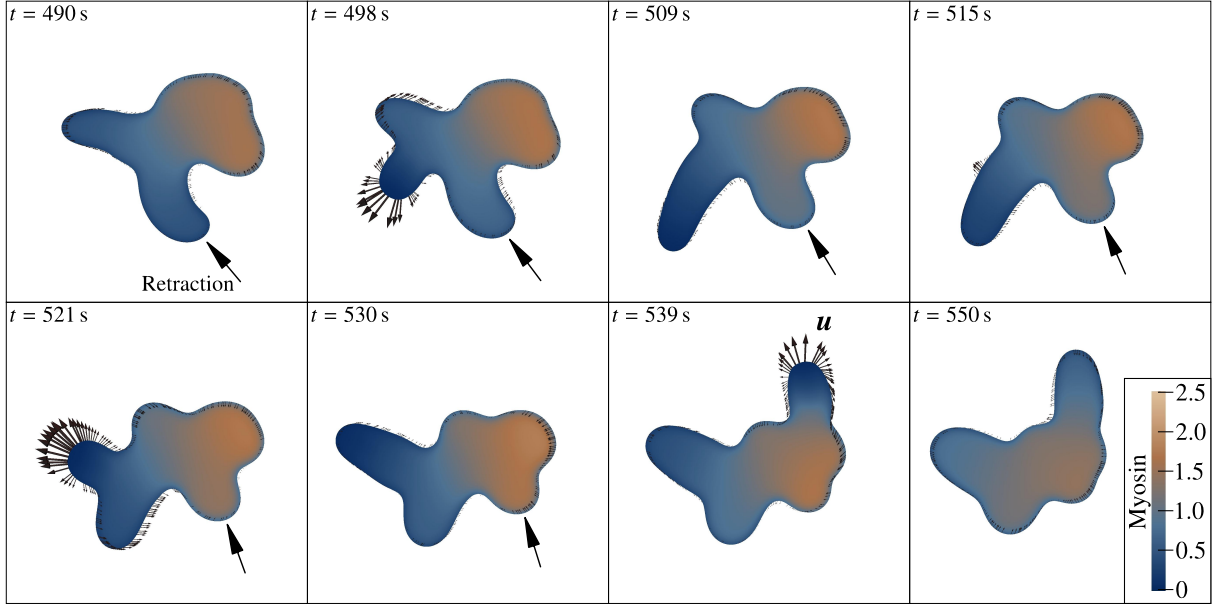
Figure 20: Amoeboid cellular motion. *Dictyostelium* free movement. Time evolution of the membrane's velocity and the myosin distribution. The arrows indicate the retraction of pseudopods produced by myosin and surface tension.

the penetration of the obstacle. $\boldsymbol{F}_{\mathrm{rep}}$ plays the role of a very simple contact model based on the penalty method. The ability of the cell to overcome the obstacle is enhanced by preventing pseudopods to form in the areas of the membrane that are close to the rigid obstacle. This constraint has been built into the model (see Section 2.6) and is based on experimental observations [63]. In the snapshots of the middle row the cell is relatively far from the obstacle and is migrating essentially as in an obstacle-free substrate. The bottom row shows how the cell hits the obstacle on the right hand side, and as it tries to reverse its direction, encounters the obstacle on the left hand side. Eventually, the cell manages to move downwards and escape away of the obstacles. Fig. 22 shows the membrane's velocity and the myosin distribution at the same time steps. It may be observed that the membrane's velocity is very small close to the obstacles due to the absence of protrusive forces.

### 4.3.3. Amoeboid migration in a three-dimensional fibrous environment

Although many experimental studies of cellular migration are performed on planar substrates, most cells migrate within the extracellular matrix – an intricate network made of fibrous proteins. The cell attaches to the fibers through integrin-mediated junctions. In turn, the fibers deform and might also get degraded due to chemicals secreted by the cell. The simulations presented in this section do not aim at reproducing this phenomenon, but rather, at proposing a much simpler scenario that is computable with the model we developed. In our simulations, the deformable fibers are replaced by rigid obstacles with fibrous geometry. The distance between fibers is probably larger than in the extracellular matrix and fiber degradation is not considered. In spite of all these assumptions, we believe that these simulations are the most realistic three-dimensional computations of cellular amoeboid motion that have been reported on heretofore. To make the problem computable we also had to modify the values of some of the parameters. We modified $\varphi$ and $\varepsilon_f$ to increase, respectively, the effective membrane thickness and the F-actin length scale. This allowed us to use coarser meshes. We have also changed the penalty constant $\alpha$ to adapt it to 3D computations ($\alpha$ is a computational parameter that depends on the number of spatial dimensions). Finally, we reduced $\bar{\eta}_m$ and $\bar{\eta}_f$ to adjust the contractile and protrusive velocities to biological values in 3D moving cells. The parameter values used in the 3D simulation are listed in Table 3. The computational domain is $\overline{\Omega} = [0, L]^3$ with $L = 32\,\mu$m. We assume periodic boundary conditions is all directions. We used 100 $C^1$-quadratic elements in each direction. The initial conditions are the same as in the previous examples of amoeboid motion, but the cell is centered at the point $\{16, 16, 16\}^T$ and has radius $r_c = 7\,\mu$m. Fig. 23 shows snapshots of the moving cell with the membrane colored according to the activator
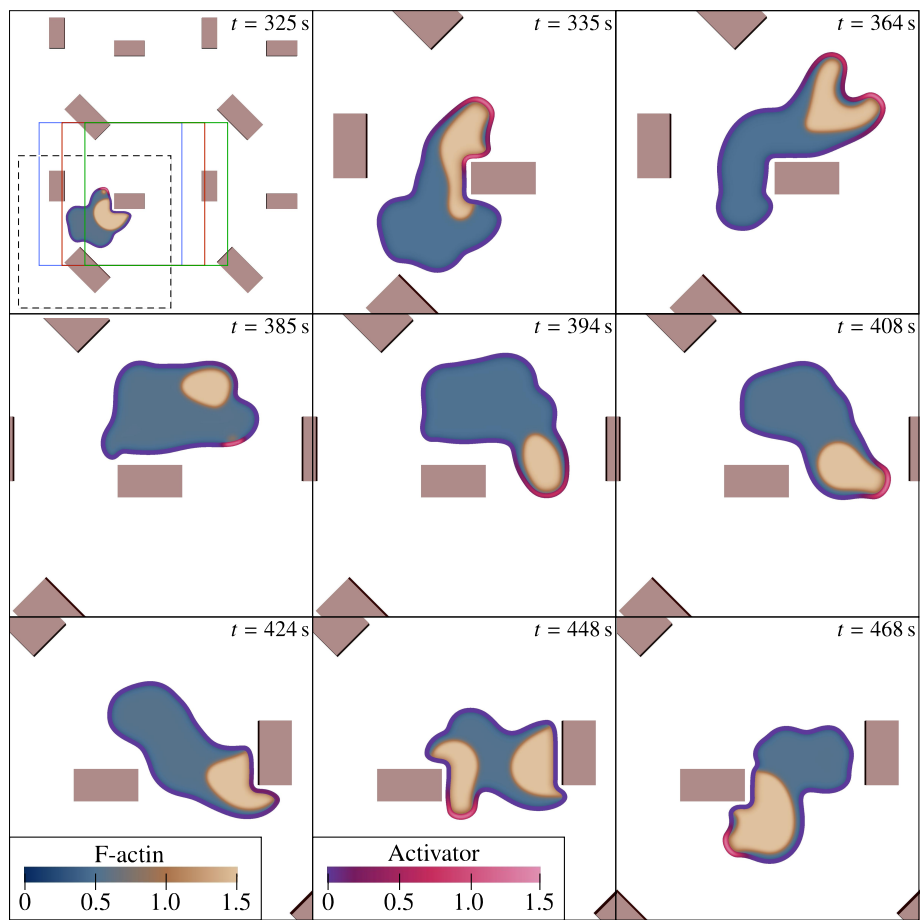
Figure 21: Amoeboid cellular motion. *Dictyostelium* migration on a planar surface with obstacles. Time evolution of the F-actin and activator concentrations.
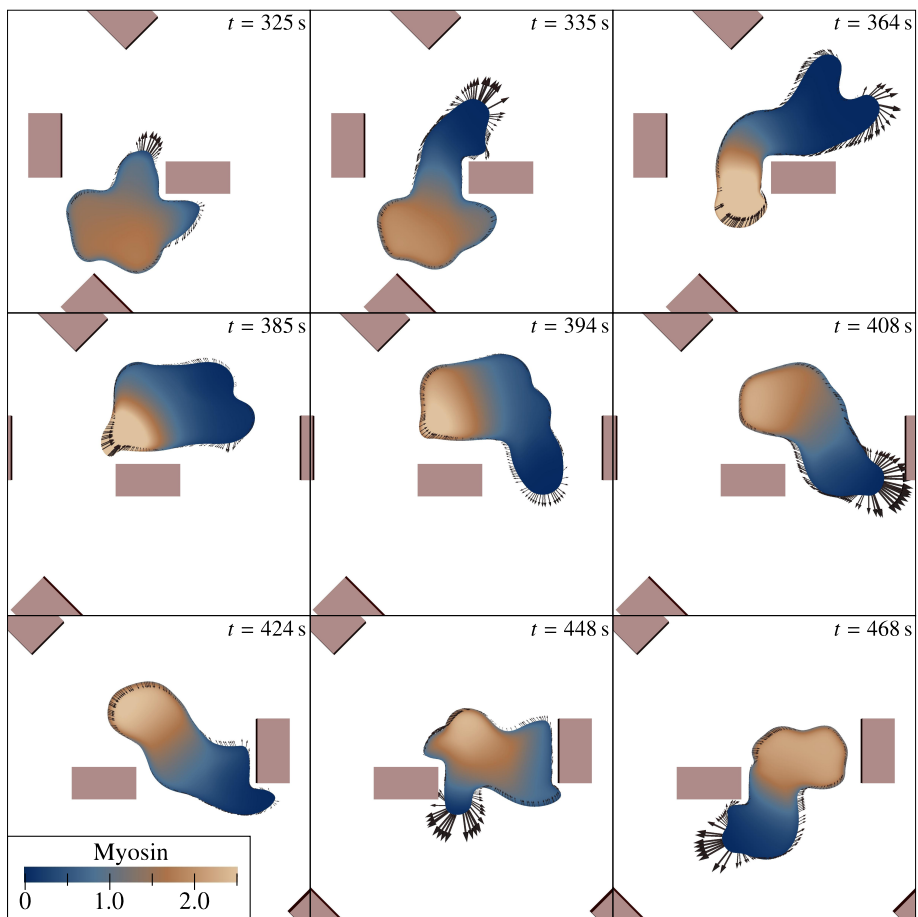
Figure 22: Amoeboid cellular motion. *Dictyostelium* migration on a planar surface with obstacles. Time evolution of the membrane's velocity and the myosin distribution.

Table 3: Dictyostelium three-dimensional motion parameters

| Symbol | Description | Value |
|---|---|---|
| $\Gamma_\phi$ | Parameter enforcing a hyperbolic tangent profile | $0.52\,\mu\mathrm{m\,s^{-1}}$ |
| $\varepsilon$ | Phase-field interfacial length scale | $2\,\mu\mathrm{m}$ |
| $D_{\max}$ | Myosin diffusion scale | $4.16\,\mu\mathrm{m^2 s^{-1}}$ |
| $K$ | Decay rate of mysosin diffusion | $1.55\,\mu\mathrm{m^3}$ |
| $\varepsilon_f$ | Diffusive length scale of F-actin | $1.0\,\mu\mathrm{m}$ |
| $\varepsilon_g$ | Diffusive length scale of G-actin | $3.16\,\mu\mathrm{m}$ |
| $\alpha$ | Penalty parameter for actin conservation | $0.03\,\mu\mathrm{m^{-3}}$ |
| $\Gamma_f$ | F-actin mobility | $0.52\,\mathrm{s^{-1}}$ |
| $\Gamma_g$ | G-actin mobility | $0.52\,\mathrm{s^{-1}}$ |
| $D_a$ | Diffusion coefficient of activator | $0.195\,\mu\mathrm{m^2 s^{-1}}$ |
| $r_a$ | Decay rate of activator | $0.325\,\mathrm{s^{-1}}$ |
| $b_a$ | Production rate of activator | $7.8\,\mathrm{s^{-1}}$ |
| $\varphi$ | Scaling of membrane marker width | 15 |
| $a_{\max}$ | Saturation of activator | $1.5\,\mu\mathrm{m^{-2}}$ |
| $r_p$ | Radius of activator source | $1\,\mu\mathrm{m}$ |
| $\Delta T_i$ | Growth time of pseudopods | See Fig. 4(a) |
| $\Delta\tau_i$ | Time interval between pseudopods | See Fig. 4(b) |
| $\mu$ | Dynamic viscosity coefficient | $1500\,\mathrm{pN\,s\,\mu m^{-2}}$ |
| $\lambda$ | Bulk viscosity coefficient | $-500\,\mathrm{pN\,s\,\mu m^{-2}}$ |
| $\bar{\eta}_m$ | Strength of contractile forces | $9.945\,\mathrm{pN\,\mu m}$ |
| $A$ | Range of contractile forces | 0.4117 |
| $\bar{\eta}_f$ | Strength of protrusive forces | $1.098\cdot10^4\,\mathrm{pN\,\mu m^3}$ |
| $B$ | Range of protrusive forces | 0.07659 |
| $\varsigma$ | Substrate friction coefficient | $0.7\,\mathrm{pN\,s\,\mu m^{-4}}$ |
| $\gamma$ | Surface tension coefficient | $78\,\mathrm{pN\,\mu m^{-1}}$ |
| $\eta_{\mathrm{rep}}$ | Strength of repulsive forces | $4550\,\mathrm{pN}$ |
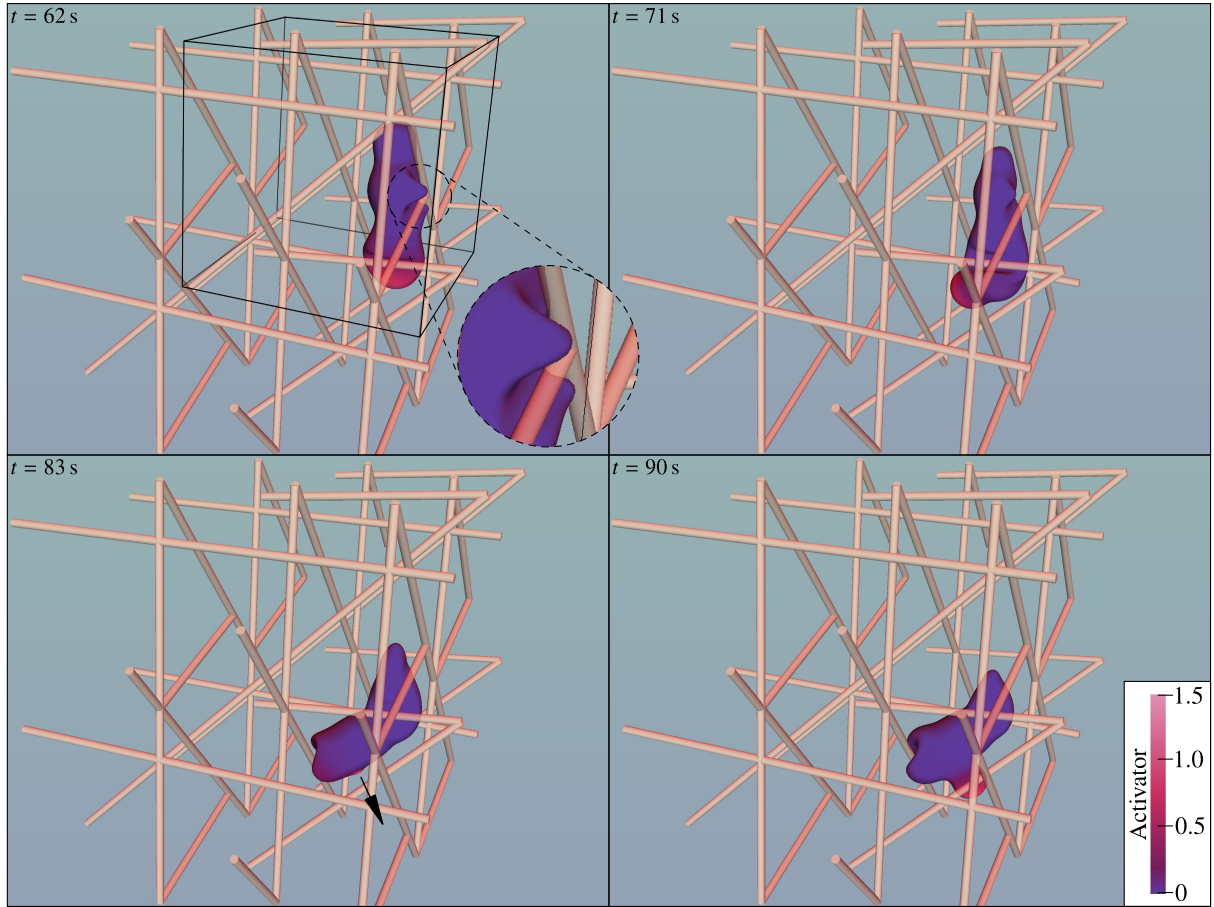
Figure 23: Amoeboid migration in a three-dimensional fibrous network. Activator distribution on the cell's membrane at $t = 62$, 71, 83, and 90 s. The top left panel shows a box that represents the actual computational domain, which has been periodically extended for visualization purposes. The arrow in the bottom left panel indicates the emergence of a new pseudopod.

concentration. The fibers (brown color) have been assumed to be straight and have a random spatial distribution and orientation. The images show how high concentrations of activator at the membrane give rise to the growth of new pseudopods as in the 2D examples. It may also be observed how the cell deforms locally to adapt to the fibrous environment (see, e.g., the zoom at the right-hand side of the top-left panel). We believe that such a strong cell deformation might not be realistic and may be attributed to our assumption of undeformable fibers. Nevertheless, the image illustrates the interaction between the cell and the obstacles. Fig. 24 shows the cell at the same times with a different perspective. The membrane is represented by a semi-transparent pink surface that allows to see the cell's interior. The surfaces inside the cell are defined by the equation $\rho_f = 1$ and represent pseudopods. This image shows how the model allows to visualize the 3D structure of pseudopods. Fig. 25 shows the evolution of the myosin distribution throughout the simulation. The highest concentrations are found in the back of the cell as in the 2D examples.

## 5. Conclusions

We proposed a phase-field model of cell migration. The model accounts for a membrane-bound species that interacts with the actin and myosin present in the cytosol. From a mechanical point of view, the cell's membrane is modeled as a vesicle and the cytosol as a viscous Newtonian fluid.
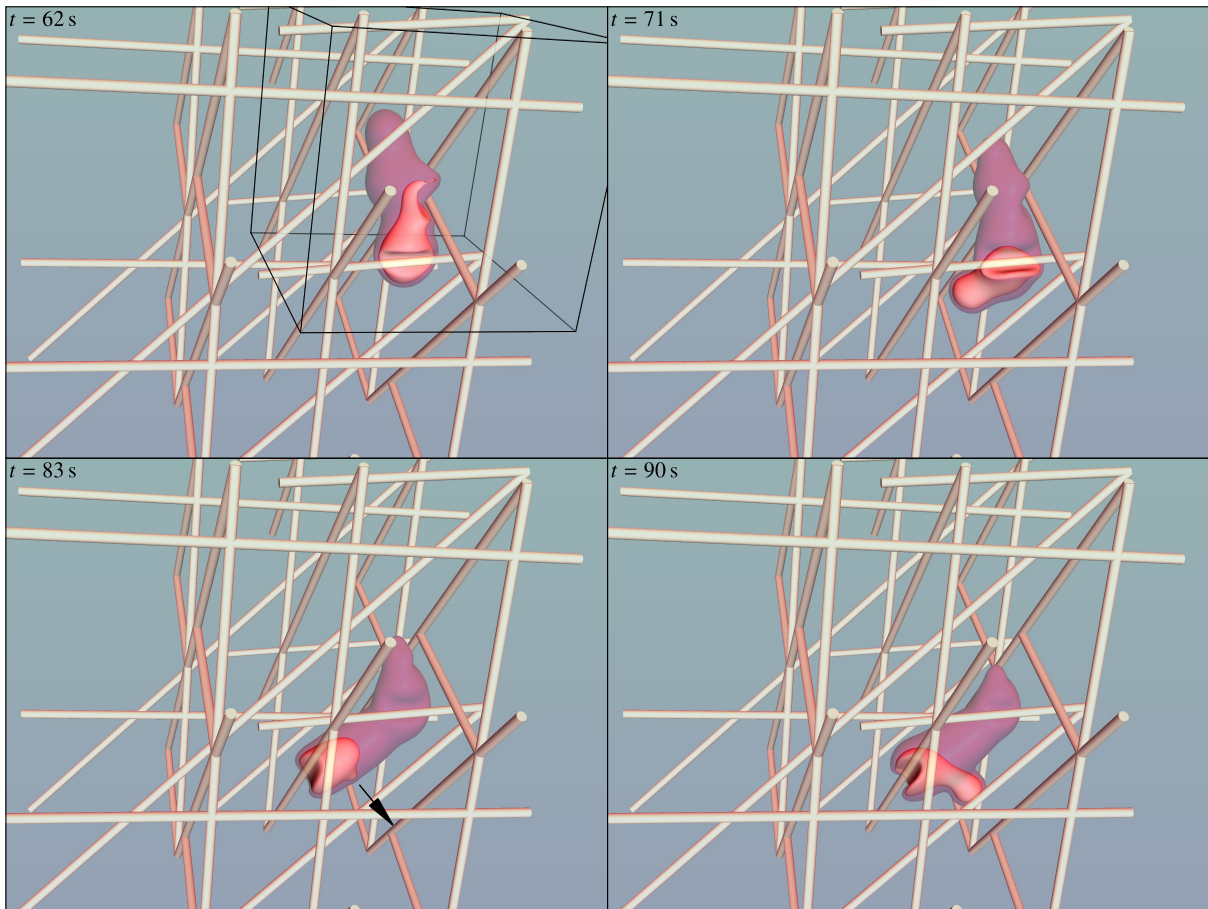
34

Figure 24: Amoeboid migration in a three-dimensional fibrous network. The cell's membrane is represented by a semi-transparent pink surface. The internal surface, defined by $\rho_f = 1$, represents the pseudopods. The top left panel shows a box that represents the actual computational domain, which has been periodically extended for visualization purposes. The arrow in the bottom left panel indicates the emergence of a new pseudopod.
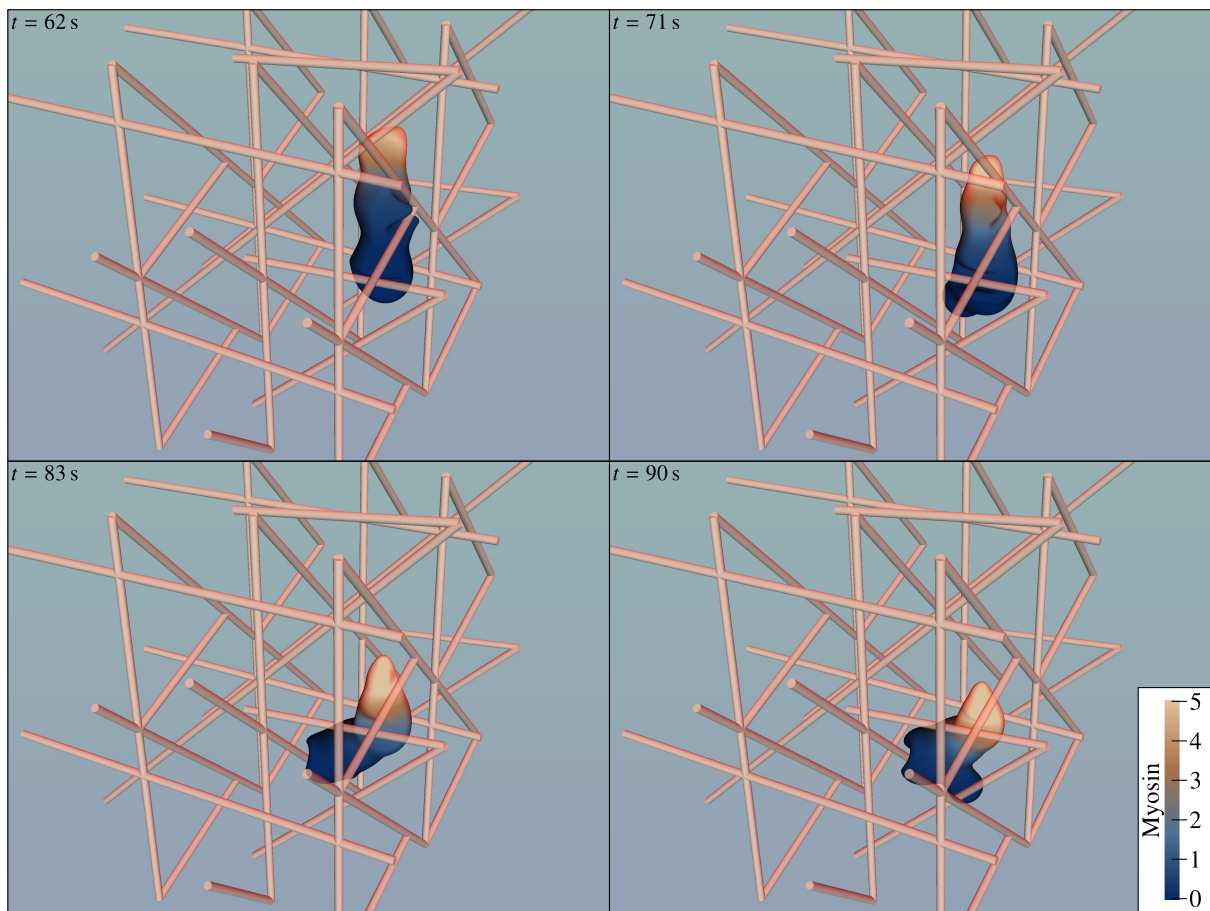
Figure 25: Amoeboid migration in a three-dimensional fibrous network. The snapshots show the time evolution of myosin concentration on the cell's surface. The computational domain is orientes as in Fig. 23.

The discretization of the model poses significant challenges to conventional numerical schemes, such as, e.g., solving equations on moving and deformable domains or approximating higher-order differential operators. The first challenge is addressed utilizing the diffuse domain method, which allows to use a fixed mesh only. The second one is handled through the use of globally continuous splines constructed using the concept of isogeometric analysis.

We applied the model to mesenchymal and amoeboid cellular motion. The simpler case of mesenchymal migration produces stationary states of motion that are in good agreement with experiments. We performed simulations of amoeboid motion on planar surfaces with and without obstacles. In all cases, the model predicted realistic dynamics. We performed a 3D simulation within a fibrous network of obstacles. We believe this simulation may constitute an initial step toward the computational study of cellular migration in the extracellular matrix.

Our model opens a number of new opportunities to study cell migration computationally. A simple way to extend the theory would be to consider deformable obstacles. This would be of special interest for the 3D simulation in a fibrous network because it would lead to be a more realistic representation of the extracellular matrix. The model can also be extended to account for chemotactic or blebbing migration.

## Acknowledgments

## References

[1] B.-C. Chen, W. R. Legant, K. Wang, L. Shao, D. E. Milkie, M. W. Davidson, C. Janetopoulos, X. S. Wu, J. A. Hammer III, Z. Liu, B. P. English, Y. Mimori-Kiyosue, D. P. Romero, A. T. Ritter, J. Lippincott-Schwartz, L. Fritz-Laylin, R. Dyche Mullins, D. M. Mitchell, J. N. Bembenek, A.-C. Reymann, R. Böhme, S. W. Grill, J. T. Wang, G. Seydoux, U. Serdar Tulu, D. P. Kiehart, E. Betzig, Lattice light-sheet microscopy: Imaging molecules to embryos at high spatiotemporal resolution, Science 346 (2014) 1257998.

[2] P. Friedl, K. Wolf, Tumour-cell invasion and migration: diversity and escape mechanisms, Nat. Rev. Cancer 3 (2003) 362–374.

[3] P. J. M. Van Haastert, P. N. Devreotes, Chemotaxis: signalling the way forward, Nat. Rev. Mol. Cell Biol. 5 (2004) 626–634.

[4] H. Gomez, K. van der Zee, Computational phase-field modeling, Encyclopedia of Computational Mechanics, (2016) accepted for publication.

[5] J. Liu, C. M. Landis, H. Gomez, T. J. R. Hughes, Liquid-vapor phase transition: Thermomechanical theory, entropy stable numerical formulation, and boiling simulations, Comput. Methods Appl. Mech. Engrg. 297 (2015) 476–553.

[6] R. P. Dhote, H. Gomez, R. N. V. Melnik, J. Zu, Shape memory alloy nanostructures with coupled dynamic thermo-mechanical effects, Comput. Phys. Commun. 192 (2015) 48–53.

[7] D. Schillinger, L. Dede', M. A. Scott, J. A. Evans, M. J. Borden, E. Rank, T. J. R. Hughes, An isogeometric design-through-analysis methodology based on adaptive hierarchical refinement of NURBS, immersed boundary methods, and T-spline CAD surfaces, Comput. Methods Appl. Mech. Engrg. 249-250 (2012) 116–150.

[8] X. Li, J. Lowengrub, A. Rätz, A. Voigt, Solving PDEs in complex geometries: a diffuse domain approach, Commun. Math. Sci. 7 (2009) 81–107.

[9] M. J. Potel, S. A. Mackay, Preaggregative cell motion in Distyostelium, J. Cell Sci. 36 (1979) 281–309.

[10] M. H. Gail, C. W. Boone, The locomotion of mouse fibroblasts in tissue culture, Biophys. J. 10 (1970) 980–993.

[11] D. Rugar, P. Hansma, Atomic force microscopy, Phys. Today 43 (1990) 23–30.

[12] D. E. Discher, P. Janmey, Y.-L. Wang, Tissue cells feel and respond to the stiffness of their substrate, Science 310 (2005) 1139–1143.

[13] P. Friedl, K. Wolf, Plasticity of cell migration: a multiscale tuning model, J. Cell Biol. 188 (2009) 11–19.

[14] T. Lämmermann, M. Sixt, Mechanical modes of 'amoeboid' cell migration, Curr. Opin. Cell Biol. 21 (2009) 636–644.

[15] M. Vicente-Manzanares, K. Newell-Litwa, A. I. Bachir, L. A. Whitmore, A. R. Horwitz, Myosin IIA/IIB restrict adhesive and protrusive signaling to generate front-back polarity in migrating cells, J. Cell Biol. 193 (2011) 381–396.

[16] M. Bergert, S. D. Chandradoss, R. A. Desai, E. Paluch, Cell mechanisc control rapid transitions between blebs and lamellipodia during migration, Proc. Natl. Acad. Sci. U.S.A. 109 (2012) 14434–14439.

[17] C. K. Choi, M. Vicente-Manzanares, J. Zareno, L. A. Whitmore, A. Mogilner, A. R. Horwitz, Actin and $\alpha$-actinin orchestrate the assembly and maturation of nascent adhesions in a myosin II motor-independent manner, Nat. Cell Biol. 10 (2008) 1039–1050.

[18] S. Li, J.-L. Guan, S. Chien, Biochemistry and biomechanics of cell motility, Annu. Rev. Biomed. Eng. 7 (2005) 105–150.

[19] A. Elosegui-Artola, R. Oria, Y. Chen, A. Kosmalska, C. Perez-Gonzalez, N. Castro, C. Zhu, X. Trepat, P. Roca-Cusachs, Mechanical regulation of a molecular clutch defines force transmission and transduction in response to matrix rigidity, Nat. Cell Biol. 18 (2016) 540–548.

[20] E. T. Roussos, J. S. Condeelis, A. Patsialou, Chemotaxis in cancer, Nat. Rev. Cancer 11 (2011) 573–587.

[21] T. Lecuit, P.-F. Lenne, Cell surface mechanics and the control of cell shape, tissue patterns and morphogenesis, Nat. Rev. Mol. Cell Biol. 8 (2007) 633–644.

[22] L. Cardamone, A. Laio, V. Torre, R. Shahapure, A. DeSimone, Cytoskeletal actin networks in motile cells are critically self-organized systems synchronized by mechanical interactions, Proc. Natl. Acad. Sci. U.S.A. 108 (2011) 13978–13983.

[23] C. Borau, T. Kim, T. Bidone, J. M. Garcia-Aznar, R. D. Kamm, Dynamic mechanisms of cell rigidity sensing: insights from a computational model of actomyosin networks, PLoS ONE 7 (2012) e49174.

[24] S. Walcott, S. X. Sun, A mechanical model of actin stress fiber formation and substrate elasticity sensing in adherent cells, Proc. Natl. Acad. Sci. U.S.A. 107 (2010) 7757–7762.

[25] H. Meinhardt, Orientation of chemotactic cells and growth cones: models and mechanisms, J. Cell Sci. 112 (1999) 2867–2874.

[26] A. Levchenko, P. A. Iglesias, Models of eukaryotic gradient sensing: application to chemotaxis of amoebae and neutrophils, Biophys. J. 82 (2002) 50–63.

[27] D. Shao, W.-J. Rappel, H. Levine, Computational model for cell morphodynamics, Phys. Rev. Lett. 105 (2010) 108104.

[28] D. Shao, H. Levine, W.-J. Rappel, Coupling actin flow, adhesion, and morphology in a computational cell motility model, Proc. Natl. Acad. Sci. U.S.A. 109 (2012) 6851–6856.

[29] J. Löber, F. Ziebert, I. S. Aranson, Modeling crawling cell movement on soft engineered substrates, Soft Matter 10 (2014) 1365–1373.

[30] A. Moure, H. Gomez, Computational model for amoeboid motion: coupling membrane and cytosol dynamics, Phys. Rev. E 94 (2016) 042423.

[31] W. Marth, A. Voigt, Signaling networks and cell motility: a computational approach using a phase field description, J. Math. Biol. 69 (2014) 91–112.

[32] A. F. M. Maree, P. Hogeweg, How amoeboids self-organize into a fruiting body: multicellular coordination in Dictyostelium discoideum, Proc. Natl. Acad. Sci. U.S.A. 98 (2001) 3879–3883.

[33] R. Rey, J. M. Garcia-Aznar, A phenomenological approach to modelling collective cell movement in 2D, Biomech. Model Mechanobiol. 12 (2013) 1089–1100.

[34] J. Xu, G. Vilanova, H. Gomez, Full-scale, three-dimensional simulation of early-stage tumor growth: the onset of malignancy, Comput. Methods in Appl. Mech. Eng. (2016) accepted for publication.

[35] C. Valero, E. Javierre, J. M. Garcia-Aznar, M. J. Gomez-Benito, Numerical modelling of the angiogenesis process in wound contraction, Biomech. Model Mechanobiol. 12 (2013) 349–360.

[36] E. L. Barnhart, K.-C. Lee, K. Keren, A. Mogilner, J. A. Theriot, An adhesion-dependent switch between mechanisms that determine motile cell shape, PLoS Biol. 9 (2011) e1001059.

[37] J. Kockelkoren, H. Levine, W.-J. Rappel, Computational approach for modeling intra- and extracellular dynamics, Phys. Rev. E 68 (2003) 037702.

[38] K. K. Subramanian, A. Narang, A mechanistic model for eukaryotic gradient sensing: spontaneous and induced phosphoinositide polarization, J. Theor. Biol. 231 (2004) 49–67.

[39] W. K. Liu, Y. Liu, D. Farrell, L. Zhang, X. S. Wang, Y. Fukui, N. Patankar, Y. Zhang, C. Bajaj, J. Lee, J. Hong, X. Chen, H. Hsu, Immersed finite element method and its applications to biological systems, Comput. Methods in Appl. Mech. Eng. 195 (2006) 1722–1749.

[40] H. Casquero, C. Bona-Casas, H. Gomez, A NURBS-based immersed methodology for fluid-structure interaction, Comput. Methods in Appl. Mech. Eng. 284 (2015) 943–970.

[41] W. Strychalski, C. A. Copos, O. L. Lewis, R. D. Guy, A poroelastic immersed boundary method with applications to cell biology, J. Comput. Phys. 282 (2015) 77–97.

[42] I. L. Novak, F. Gao, Y.-S. Choi, D. Resasco, J. C. Schaff, B. M. Slepchenko, Diffusion on a curved surface coupled to diffusion in the volume: application to cell biology, J. Comput. Phys. 226 (2007) 1271–1290.

[43] I. Hecht, M. L. Skoge, P. G. Charest, E. Ben-Jacob, R. A. Firtel, W. F. Loomis, H. Levine, W.-J. Rappel, Activated membrane patches guide chemotactic cell motility, PLoS Comput. Biol. 7 (2011) e1002044.

[44] G. MacDonald, J. A. Mackenzie, M. Nolan, R. H. Insall, A computational method for the coupled solution of reaction–difusion equations on evolving domains and manifolds: application to a model of cell migration and chemotaxis, J. Comput. Phys. 309 (2016) 207–226.

[45] I. Hecht, M. L. Skoge, P. G. Charest, E. Ben-Jacob, R. A. Firtel, W. F. Loomis, H. Levine, W.-J. Rappel, Activated membrane patches guide chemotactic cell motility, PLoS Comput. Biol. 7 (2011) e1002044.

[46] C. W. Wolgemuth, M. Zajac, The moving boundary node method: a level set-based, finite volume algorithm with applications to cell motility, J. Comput. Phys. 229 (2010) 7287–7308.

[47] B. A. Camley, Y. Zhang, Y. Zhao, B. Li, E. Ben-Jacob, H. Levine, W.-J. Rappel, Polarity mechanisms such as contact inhibition of locomotion regulate persistent rotational motion of mammalian cells con micropatterns, Proc. Natl. Acad. Sci. U.S.A. 111 (2014) 14770–14775.

[48] B. A. Camley, Y. Zhao, B. Li, H. Levine, W.-J. Rappel, Crawling and turning in a minimal reaction-diffusion cell motility model: coupling cell shape and biochemistry, arXiv preprint arXiv:1609.01764.

[49] J. Löber, F. Ziebert, I. S. Aranson, Modeling crawling cell movement on soft engineered substrates, Soft Matter 10 (2014) 1365–1373.

[50] A. Dreher, I. S. Aranson, K. Kruse, Spiral actin-polymerization waves can generate amoeboidal cell crawling, New J. Phys. 16 (2014) 055007.

[51] T. Biben, K. Kassner, C. Misbah, Phase-field approach to three-dimensional vesicle dynamics, Phys. Rev. E 72 (2005) 041921.

[52] B. A. Camley, Y. Zhao, B. Li, H. Levine, W.-J. Rappel, Periodic migration in a physical model of cells on micropatterns, Phys. Rev. Lett. 111 (2013) 158102.

[53] W. R. Holmes, L. Edelstein-Keshet, A comparison of computational models for eukaryotic cell shape and motility, PLoS Comput. Biol. 8 (2012) e1002793.

[54] A. Jilkine, L. Edelstein-Keshet, A comparison of mathematical models for polarization of single eukaryotic cells in response to guided cues, PLoS Comput. Biol. 7 (2011) e1001121.

[55] K. E. Teigen, X. Li, J. Lowengrub, F. Wang, A. Voigt, A diffuse-interface approach for modeling transport, diffusion and adsorption/desorption of material quantities on a deformable interface, Commun. Math. Sci. 4 (2009) 1009–1037.

[56] J. Parvizian, A. Düster, E. Rank, h- and p- extension for embedded domain problems in solid mechanics, Comput. Mech. 41 (2007) 121–133.

[57] B. Rubinstein, M. F. Fournier, K. Jacobson, A. B. Verkhovsky, A. Mogilner, Actin-myosin viscoelastic flow in keratocyte lamellipod, Biophys. J. 97 (2009) 1853–1863.

[58] P. B. Canham, The minimum energy of bending as a possible explanation of the biconcave shape of the human red blood cell, J. Theor. Biol. 26 (1970) 61–81.

[59] W. Helfrich, Elastic properties of lipid bilayers: theory and possible experiments, Z. Naturforsch C. 28 (1973) 693–703.

[60] E. Fried, On the relationship between supplemental balances in two theories for pure interface motion, SIAM J. Appl. Math. 66 (2006) 1130–1149.

[61] R. H. Insall, Understanding eukaryotic chemotaxis: a pseudopod-centred view, Nat. Rev. Mol. Cell Biol. 11 (2010) 453–458.

[62] L. Bosgraaf, P. J. M. Van Haastert, The ordered extension of pseudopodia by amoeboid cells in the absence of external cues, PLoS ONE 4 (2009) e5253.

[63] O. Nagel, C. Guven, M. Theves, M. Driscoll, W. Losert, C. Beta, Geometry-driven polarity in motile amoeboid cells, PLoS ONE 9 (2014) e113382.

[64] T. J. R. Hughes, J. A. Cottrell, Y. Bazilevs, Isogeometric analysis: CAD, finite elements, NURBS, exact geometry and mesh refinement, Comput. Methods in Appl. Mech. Eng. 194 (2005) 4135–4195.

[65] J. A. Cottrell, T. J. R. Hughes, Y. Bazilevs, Isogeometric Analysis: Toward Integration of CAD and FEA, Wiley, 2009.

[66] L. Piegl, W. Tiller, The NURBS Book, Springer, 1995.

[67] F. Calabrò, G. Sangalli, M. Tani, Fast formation of isogeometric galerkin matrices by weighted quadrature, Comput. Methods in Appl. Mech. Eng. (2016) accepted for publication.

[68] F. Auricchio, L. B. Da Veiga, T. Hughes, A. Reali, G. Sangalli, Isogeometric collocation methods, Math. Models Methods Appl. Sci. 20 (11) (2010) 2075–2107.

[69] H. Gomez, L. De Lorenzis, The variational collocation method, Comput. Methods in Appl. Mech. Eng. 309 (2016) 152–181.

[70] J. Chung, G. M. Hulbert, A time integration algorithm for structural dynamics with improved numerical dissipation: the generalized-$\alpha$ method, J. Appl. Mech. 60 (1993) 371–375.

[71] K. Jansen, C. Whiting, G. Hulbert, Generalized-$\alpha$ method for integrating the filtered Navier–Stokes equations with a stabilized finite element method, Comput. Methods Appl. Mech. Engrg. 190 (2000) 305–319.

[72] H. Gomez, V. M. Calo, Y. Bazilevs, T. J. R. Hughes, Isogeometric analysis of the Cahn–Hilliard phase-field model, Comput. Methods Appl. Mech. Engrg. 197 (2008) 4333–4352.

[73] Y. Saad, M. H. Schultz, GMRES: a generalized minimal residual algorithm for solving nonsymmetric linear systems, SIAM J. Sci. Stat. Comput. 7 (1986) 856–869.

[74] T. F. Chan, H. A. Van der Vorst, Approximate and Incomplete Factorizations, Springer, 1997.

[75] S. M. Allen, J. W. Cahn, A microscopic theory for antiphase boundary motion and its application to antiphase domain coarsening, Acta Met. 27 (1979) 1085–1095.

[76] N. Collier, L. Dalcin, V. Calo, PetIGA: high-performance isogeometric analysis, preprint arXiv:1305.4452.

[77] P. Vignal, N. Collier, V. Calo, Phase field modeling using PetIGA, Procedia Comput. Sci. 18 (2013) 1614–1623.

[78] S. Balay, S. Abhyankar, M. F. Adams, J. Brown, P. Brune, K. Buschelman, L. Dalcin, V. Eijkhout, W. D. Gropp, D. Kaushik, M. G. Knepley, L. C. McInnes, K. Rupp, B. F. Smith, S. Zampini, H. Zhang, H. Zhang, PETSc Web page, 2016. http://www.mcs.anl.gov/petsc.

[79] K. Keren, Z. Pincus, G. M. Allen, E. L. Barnhart, G. Marriott, A. Mogilner, J. A. Theriot, Mechanisms of shape determination in motile cells, Nature 453 (2008) 475–480.

[80] M. F. Fournier, R. Sauser, D. Ambrosi, J.-J. Meister, A. B. Verkhovsky, Force transmission in migrating cells, J. Cell Biol. 188 (2010) 287–297.

[81] R. Simson, E. Wallraff, J. Faix, J. Niewöhner, G. Gerisch, E. Sackmann, Membrane bending modulus and adhesion energy of wild-type and mutant cells of Dictyostelium lacking talin or cortexillins, Biophys. J. 74 (1998) 514–522.

[82] R. Dimova, Recent developments in the field of bending rigidity measurements on membranes, Adv. Colloid Interface Sci. 208 (2014) 225–234.

[83] E. L. Barnhart, G. M. Allen, F. Jülicher, J. A. Theriot, Bipedal locomotion in crawling cells, Biophys. J. 98 (2010) 933–942.